Mon. Not. R. Astron. Soc. **394,** 1758–1774 (2009) doi:10.1111/j.1365-2966.2009.14475.x

3D modelling of the colliding winds in η Carinae – evidence for radiative inhibition

E. R. Parkin,[1]★ J. M. Pittard,[1] M. F. Corcoran,[2,3] K. Hamaguchi[2,4] and I. R. Stevens[5]

[1] *School of Physics and Astronomy, The University of Leeds, Woodhouse Lane, Leeds LS2 9JT*
[2] *CRESST and X-ray Astrophysics Laboratory, NASA/GSFC, Greenbelt, MD 20771, USA*
[3] *Universities Space Research Association, 10211 Wisconsin Circle, Suite 500 Columbia, MD 21044, USA*
[4] *Department of Physics, University of Maryland, Baltimore County, 1000 Hilltop Circle, Baltimore, MD 21250, USA*
[5] *School of Physics and Astronomy, University of Birmingham, Edgbaston, Birmingham B15 2TT*

Accepted 2009 January 7. Received 2009 January 6; in original form 2008 November 19

ABSTRACT

The X-ray emission from the supermassive star η Car is simulated using a 3D model of the wind–wind collision. In the model the intrinsic X-ray emission is spatially extended and energy dependent. Absorption due to the unshocked stellar winds and the cooled post-shock material from the primary LBV star is calculated as the intrinsic emission is ray traced along multiple sightlines through the 3D spiral structure of the circumstellar environment. The observable emission is then compared to available X-ray data, including the light curve observed by the *Rossi X-ray Timing Explorer* (*RXTE*) and spectra observed by *XMM–Newton*. The orientation and eccentricity of the orbit are explored, as are the wind parameters of the stars and the nature and physics of their close approach. Our modelling supports a viewing angle with an inclination of $\simeq 42°$, consistent with the polar axis of the Homunculus nebula, and the projection of the observer's line of sight on to the orbital plane has an angle of $\simeq 0°$–$30°$ in the prograde direction on the apastron side of the semimajor axis.

However, there are significant discrepancies between the observed and model light curves and spectra through the X-ray minimum. In particular, the hard flux in our synthetic spectra is an order of magnitude greater than observed. This suggests that the hard X-ray emission near the apex of the wind–wind collision region (WCR) 'switches off' from periastron until two months afterwards. Further calculations reveal that radiative inhibition significantly reduces the pre-shock velocity of the companion wind. As a consequence the hard X-ray emission is quenched, but it is unclear whether the long duration of the minimum is due solely to this mechanism alone. For instance, it is possible that the collapse of the WCR on to the surface of the companion star, which would be aided by significant inhibition of the companion wind, could cause an extended minimum as the companion wind struggles to re-establish itself as the stars recede. For orbital eccentricities, $e \lesssim 0.95$, radiative braking prevents a wind collision with the companion star's surface. Models incorporating a collapse/disruption of the WCR and/or reduced pre-shock companion wind velocities bring the predicted emission and the observations into much better agreement.

Key words: hydrodynamics – stars: early-type – binaries: close – stars: individual: η Carinae – stars: winds, outflows – X-rays: stars.

1 INTRODUCTION

The supermassive star η Car provides a unique laboratory for the study of massive star evolution. Situated in the Carina nebula, at a distance of 2.3 kpc (Davidson & Humphreys 1997), η Car has been identified as a luminous blue variable (LBV) star, a short-lived ($\sim 10^4$ yr) phase in the life of a massive star occurring after the main sequence and preceding the Wolf–Rayet phase. η Car is believed to have a current mass of $\simeq$80–120 $\mathrm{M_{\odot}}$, and an initial mass $\gtrsim 150\,\mathrm{M_{\odot}}$ (Hillier et al. 2001). Over the past 200 yr episodes of rapid mass-loss have been observed from the star, and in 1843 the 'Great Eruption' ejected more than 10 $\mathrm{M_{\odot}}$ of matter (Smith et al. 2003b) from the central object over a $\sim$20 yr period,

---

★E-mail: phy1erp@leeds.ac.uk

forming the bipolar nebula known as the Homunculus. In the 1890s a further smaller eruption with a mass-loss of $\sim 1\,\mathrm{M_\odot}$ produced the Little Homunculus (Ishibashi et al. 2003). The central object is now shrouded by a large amount of dense absorbing gas and hot and cold dust which makes observations at optical and ultraviolet wavelengths difficult.

Although many questions still remain about the nature of this system, a periodicity of ∼5.5 yr in the X-ray, radio, millimetre, infrared and optical is now clearly established (Damineli et al. 2008a, and references therein), and has provided strong evidence for the presence of a binary companion. With an orbital eccentricity of $\simeq 0.9$ (Smith et al. 2004), the stellar separation at periastron may only be $\simeq 1.6$ au (with a semimajor axis of 16.64 au; Hillier et al. 2001). The radius of the primary star is unclear but it may be as high as 1 au (Damineli 1996). The companion star has remained very elusive, but is thought to have a mass $\sim 30\,\mathrm{M_\odot}$, and to be either an O star or a WR star (Pittard & Corcoran 2002, hereafter PC02). In this paper the more massive star, the LBV, will be referred to as the primary, and the smaller companion will be referred to as the secondary. Typical orbital and stellar parameters for the binary system are noted in Table 1.

While the binary model is now commonly accepted, the orientation of the system, the mass-loss rates of the stars, and the key physics occurring around periastron passage are much more controversial. Most works favour the secondary star moving behind the primary around periastron (e.g. Damineli 1996; Pittard et al. 1998; Corcoran et al. 2001; Corcoran 2005; Akashi, Soker & Behar 2006; Hamaguchi et al. 2007; Nielsen et al. 2007; Henley et al. 2008; Okazaki et al. 2008), though some others favour a system orientated such that the secondary star is positioned in front of the primary during periastron passage (Falceta-Gonçalves, Jatenco-Pereira & Abraham 2005; Kashi & Soker 2007), or at quadrature (Ishibashi 2001; Smith et al. 2004). Estimates of the mass-loss rate of the primary star range from a few $\times 10^{-4}$ (Corcoran et al. 2001; PC02) to a few $\times 10^{-3}\,\mathrm{M_\odot\,yr^{-1}}$ (Hillier et al. 2001; van Boekel et al. 2003). Observations of the reflected emission from the Homunculus by Smith et al. (2003a) revealed a higher degree of absorption at high latitudes, implying a higher rate of mass-loss from the primary star near the poles. In contrast, the X-ray emission from the WCR is most sensitive to the mass-loss near the orbital plane. If the orbital plane is aligned with the equatorial region of the winds this may explain some of the difference in the estimated mass-loss rates.

The X-ray emission has proved to be extremely useful for deciphering the complex phenomena of η Car, because it is relatively unattenuated and can be used to probe deep into the centre of the system. The keV X-ray emission displays a dominantly thermal spectrum, and indicates the presence of hot shocked gas at a temperature of $\sim 10^7$–10^8 K. While there are several possible methods for generating high-temperature plasma, the X-ray light curve provides strong support to the binary scenario, where the X-ray emission naturally arises from the high-speed collision of the winds in a massive binary system (e.g. Stevens, Blondin & Pollock 1992; Pittard & Stevens 1997; Pittard 2007). Since the LBV wind is slow, and cannot be shock heated to high temperatures, the X-ray emission in this scenario must arise from a much faster companion wind.

Fits to a grating spectrum from the *Chandra* satellite obtained mass-loss rates and terminal wind speeds of $2.5 \times 10^{-4}\,\mathrm{M_\odot\,yr^{-1}}$ and $500\,\mathrm{km\,s^{-1}}$ for the primary star, and $1.0 \times 10^{-5}\,\mathrm{M_\odot\,yr^{-1}}$ and $3000\,\mathrm{km\,s^{-1}}$ for the secondary star (PC02). The spectrum was attained near apastron, when 2D hydrodynamic simulations (which ignore orbital motion) give a good description of the WCR.

A particularly interesting feature of the X-ray emission is the long and deep minimum which coincides with periastron passage of the stars. During this interval emission from the system undergoes dramatic variations across a broad range of wavelengths, with high excitation lines displaying a rapid reduction or 'collapse' in intensity (Damineli et al. 2008b). We construct a 3D model of the WCR in which rapid and large changes in the structure occur during periastron passage. The model allows us to investigate the X-ray emission throughout the entire orbit, so that the orbital orientation, the eccentricity, and the wind parameters of the stars can be determined. We then explore the physics of the WCR during periastron passage. The layout of this paper is as follows. Section 2 discusses a number of scenarios which have been suggested to explain the behaviour of the X-ray minimum; Section 3 contains a brief description of the dynamic model developed by Parkin & Pittard (2008, hereafter

Table 1. Assumed parameters for η Car. $\eta = \dot{M}_2 v_{\infty 2}/\dot{M}_1 v_{\infty 1}$ is the wind momentum ratio and a is the semimajor axis of the orbit. References are as follows: 1 = Davidson & Humphreys (1997), 2 = Hillier et al. (2001), 3 = PC02, 4 = Corcoran (2005), 5 = Corcoran & Hamaguchi (2007). After an extensive parameter space exploration we found that a composite (ISM + nebula) column density (between the observer at Earth and the edge of the simulation box, 1500 au from the stars) of $1 \times 10^{22}\,\mathrm{cm^{-2}}$ provided better fits to the X-ray flux in the soft band (2–5 keV). This value is consistent with, but slightly lower than, the value of $5 \times 10^{22}\,\mathrm{cm^{-2}}$ derived by Hamaguchi et al. (2007) for the 'the absorption beyond the central source', which likely represents the absorption column between the secondary star at apastron and the observer at earth. R_* is taken to be the radius of the gravitationally bound region of the star; for the primary star the photosphere will exist somewhere in the stellar wind.

Parameter	Primary	Secondary	System	Reference
M ($\mathrm{M_\odot}$)	120	30		2
R_* ($\mathrm{R_\odot}$)	100	20		5
$\dot{M}$($10^{-5}\,\mathrm{M_\odot\,yr^{-1}}$)	25	1		3
v_∞ ($\mathrm{km\,s^{-1}}$)	500	3000		3
η			0.24	3
a (au)			16.64	2
Orbital period (d)			2024	4
Eccentricity (e)			0.9	4
Distance (kpc)			2.3	1
ISM + nebula column ($10^{22}\,\mathrm{cm^{-2}}$)			1	

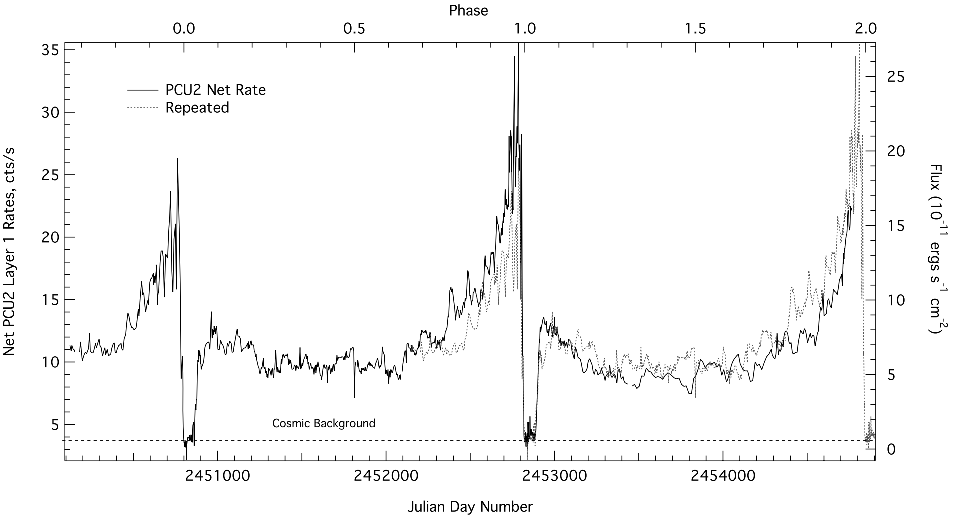

Figure 1. The 2–10 keV X-ray light curve of η Car corrected for instrumental background over two periastron passages taken with the *RXTE* satellite (Corcoran 2005). The data from ~1996 to 2003.5 (dotted) have been superimposed over the 2002–present data for comparison. For the majority of the orbit the flux is broadly constant. Prior to periastron passage there is a distinctive rise to maximum, then a sharp fall to a deep minimum. There is a noticeable difference between the peak magnitudes prior to the minimum of the last two cycles. The dotted horizontal line is an estimate of the flux due to cosmic background which contaminates the *RXTE*/PCU2 field of view.

PP08) which we apply to η Car in Section 4; Section 5 examines a number of mechanisms which may be important for bringing about the X-ray minimum; and Section 6 concludes and outlines possible future directions.

2 THE X-RAY MINIMUM

2.1 Observations

The *Rossi X-ray Timing Explorer* (*RXTE*) has observed η Car since 1996, so that data over more than two orbital cycles are now available. The X-ray light curve is shown in Fig. 1. Following apastron, there is a gradual increase in emission over approximately 2 yr, followed by a rapid decline to a deep minimum which lasts for approximately 60 d ($\simeq 0.03$ in orbital phase), then a shallower egress out of the minimum to a roughly constant luminosity prior to its gradual rise again in the next cycle (Ishibashi et al. 1999; Corcoran et al. 2001; Corcoran 2005).

XMM–Newton spectra analysed by Hamaguchi et al. (2007) showed that the flux in the 2–10 keV range at the start of the minimum was 0.7 per cent of the maximum value observed by *RXTE* before the minimum. Surprisingly, the flux in the latter half of the minimum increases by a factor of 5 from the lowest observed value, indicating that the minimum has two states. Some of the observed X-ray flux during the minimum is emission from an earlier orbital phase which is scattered by the Homunculus (Corcoran et al. 2004).

2.2 Possible explanations

There are currently a number of possible explanations for the minimum in the X-ray light curve which may, or may not, be mutually exclusive.

(i) *The eclipse model*: The region of the WCR responsible for emitting 0.1–10 keV X-rays may be fully occulted by the primary star itself, or by its dense, optically thick wind (i.e. a wind eclipse) if the secondary moves behind the primary star at periastron. The lack of variation in the plasma temperature measured in the *XMM–Newton* spectra during the minimum is supportive of an eclipse of the source, in which case residual emission arises from regions further downstream. Okazaki et al. (2008) find that pile-up of the dense primary wind after periastron can cause an extended minimum via a wind eclipse. On the other hand, the deformation of the Fe XXV profile and the relatively weak fluorescence Fe line intensity during the minimum may suggest an intrinsic fading of the X-ray emissivity (Hamaguchi et al. 2007).

(ii) *Increased mass-loss*: LBV's exhibit variability on a number of time-scales (e.g. de Groot, Sterken & van Genderen 2001), and are known to go through eruptive phases where large amounts of stellar material are ejected into the surrounding interstellar medium (ISM). The primary star may be undergoing S Dor-like fluctuations (van Genderen & Sterken 2007), which may reach a maximum around periastron with a shell-ejection event (such an event was proposed by Davidson & Humphreys 1997, as an alternative to the binary eclipse model for explanation of the X-ray minimum).

Theoretical work on tidal interactions in binary systems shows that tidal oscillations may result in a phase of increased non-spherical mass-loss (Moreno, Koenigsberger & Toledano 2005; Kashi & Soker 2008, and references therein). Corcoran et al. (2001) found that incorporating a factor of ~20 increase in the primary star mass-loss rate for $\delta\phi \sim 0.04$ improved the fit to the duration of the minimum. High-velocity absorption lines (~750 km s^{-1} for He I λ6678) observed by Stahl et al. (2005) around periastron in the reflected emission from the Homunculus nebula may be evidence of a period of increased mass-loss.

(iii) *Shut-down of the companion's wind*: If the WCR moves into the acceleration region of the secondary's wind (due to contraction of the stellar separation), a stable momentum balance may be lost, resulting in the primary's wind overwhelming the secondary's wind and causing the WCR to collapse on to the surface of the secondary star. This may be aided by the radiative inhibition (Stevens & Pollock 1994) or braking (Gayley, Owocki & Cranmer 1997) of the secondary star's wind at periastron due to the high stellar luminosity of the primary star ($\simeq$ a few $\times 10^6\ L_\odot$). Evidence for a collapse of the WCR on to the secondary star exists in the behaviour of the highly ionized lines around the minimum (Damineli et al. 2008b). This possibility, and the potential occurrence of accretion of the primary wind by the companion star, was explored by Akashi et al. (2006).

3 THE DYNAMIC MODEL

To successfully model the X-ray minimum the motion of the shocked and unshocked gas relative to the stars must be taken into account. Unfortunately, with current computational resources, it is difficult to explore a wide range of parameter space with 3D models, even when using sophisticated grid or particle based hydrodynamic codes. The high orbital eccentricity of η Car compounds this problem, and 3D simulations of η Car have only examined a small region of parameter space to date (Pittard 2000; Okazaki et al. 2008). While both of these efforts revealed important insights into the dynamics of the WCR, only a small part of the orbit around periastron passage was simulated in Pittard (2000), while the assumption of isothermality in Okazaki et al. (2008) does not allow direct calculation of the X-ray emission.

In this paper we use a recently developed 3D dynamical model which allows efficient exploration of parameter space. A detailed description can be found in PP08 where a demonstration with lower eccentricity O + O and WR + O star binaries is given. The model uses equations from Canto, Raga & Wilkin (1996) to determine the ram-pressure balance and position of the contact discontinuity (CD) between the winds (modified by an aberration angle due to orbital motion). The flow downstream of the 'apex' of the WCR is then assumed to travel ballistically. The motion of the stars causes the contact surface to wind up and form large-scale spiral structures (Fig. 2), reminiscent of the beautiful 'pinwheel nebulae' (Tuthill et al. 2008). The shape of the WCR around periastron passage is highly distorted due to the rapid transit of the stars and the slow speed of the primary wind (Fig. 3).

The X-ray emission from the WCR is a function of the gas temperature and density. Since the dynamical model does not contain such information we use a grid-based, 2D hydrodynamical calculation of an axisymmetric WCR to obtain this. The resulting emission as a function of off-axis distance is then mapped on to the coordinate positions in the 3D dynamical model. In this way we obtain the benefit of effectively modelling the thermodynamic and hydrodynamic behaviour responsible for the production of the X-ray emission, while simultaneously accounting for the effect of the motion of the stars on the large-scale structure of the WCR and the subsequent wind attenuation. Since the hydrodynamic calculation is 2D, the computational requirements remain low.

The X-ray luminosity per unit volume is given by $\Gamma(E) = n^2 \Lambda(E, T)$, where n is the gas number density (cm^{-3}) and $\Lambda(E, T)$ is the emissivity (erg cm^3 s^{-1}) as a function of energy E and temperature T for optically thin gas in collisional ionization equilibrium. $\Lambda(E, T)$ is obtained from look-up tables calculated from the MEKAL plasma code (Liedahl, Osterheld & Goldstein 1995, and references therein), containing 200 logarithmically spaced energy bins in the range 0.1–10.0 keV, and 101 logarithmically spaced temperatures from 10^4 to 10^9 K. Solar abundances are assumed.

The orbit of the stars is modelled in the xy plane, so that viewing angles into the system can be described by the inclination angle that the line of sight makes with the z-axis, i, and the angle the projected line of sight makes with the major axis of the orbit, θ (positive values correspond to an angle subtended against the positive x-axis in the prograde direction). The components of the unit vector along the line of sight, $\underline{\hat{u}}$, are

$$u_x = \cos\theta \sin i,$$
$$u_y = \sin\theta \sin i,$$
$$u_z = \cos i.$$

To determine the observed attenuated emission ray tracing is performed through the spiral structure. Specific details of the emission and absorption calculations are now discussed.

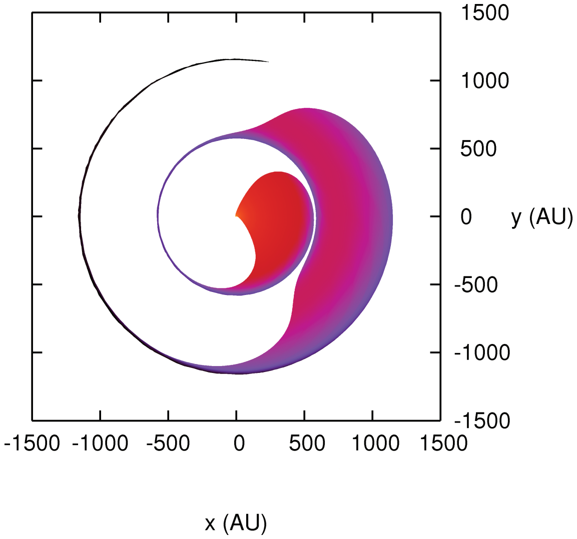

Figure 2. The large-scale structure of the CD (which separates the two winds) viewed from above the orbital plane. The white region marks the unshocked wind of the primary star. In this model the unshocked secondary wind is entirely contained within the coloured region. The primary star is located at the origin and the companion star orbits about this point. The WCR forms a spiral structure due to the orbital motion of the stars. Asymmetry in the distribution of the unshocked companion wind is caused by the highly eccentric (e = 0.9) orbit. The thinning of the coloured region towards the tail of the spiral is an artefact of the model (see PP08), due to the fact that the WCR is traced back for only two orbits. The parameters used in this simulation are noted in Table 1.

3.1 Emission from the shocked secondary wind

The importance of cooling in the WCR can be quantified using the cooling parameter (Stevens et al. 1992)

$$\chi = \frac{t_{\rm cool}}{t_{\rm esc}} = \frac{v_8^4 d_{12}}{\dot{M}_{-7}}, \qquad (1)$$

where v_8 is the pre-shock wind velocity in units of 1000 km s^{-1}, d_{12} is the distance from the star to the CD in units of 10^{12} cm, $\dot{M}_{-7}$ is the mass-loss rate of the star in units of 10^{-7} M$_\odot$ yr^{-1}, $t_{\rm cool}$ is the cooling time and $t_{\rm esc}$ is the escape time of gas out of the system ($\simeq d_{12}/c_{\rm s}$, where $c_{\rm s}$ is the post-shock sound speed). χ_1 and χ_2 are the cooling parameter for the post-shock primary and secondary winds, respectively.

In the case of η Car, the post-shock primary wind is strongly radiative ($\chi \simeq 10^{-4}$ to 10^{-2}), rapidly cools, and collapses to form a thin dense sheet. As previously noted, this wind is not expected to produce thermal X-rays above 1–2 keV as the relatively low wind speed ($v_1 \sim 500$ km s^{-1}) does not shock-heat gas to high enough temperatures. In contrast, the high velocity of the secondary's wind ($v_2 \sim 3000$ km s^{-1}) causes its post-shock flow to be adiabatic ($\chi \gtrsim 10$) around most of the orbit. To first order the entirety of the

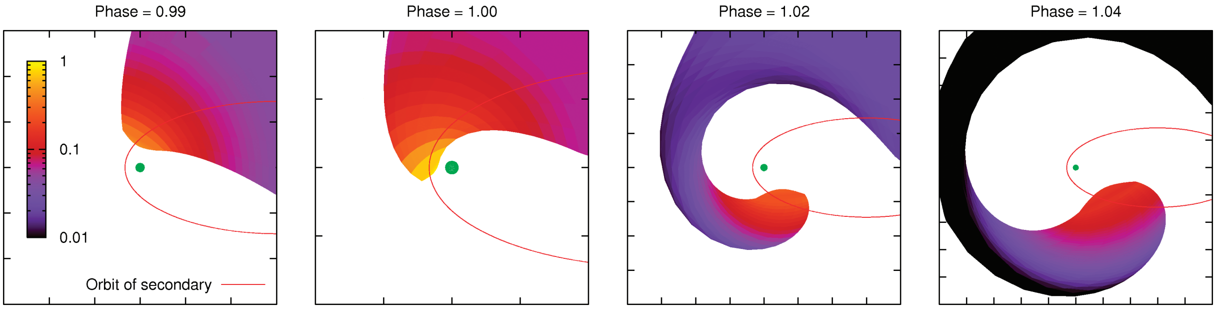

Figure 3. The structure and position of the WCR around periastron passage. The colour scale shows the SD of the post-shock primary wind in g cm^{-2}. The primary star is shown as a green circle. The tick marks on the axis mark a distance of 5 au (note the different scale of each panel). From left- to right-hand side the plots correspond to 20 d before periastron, periastron itself, and 40 and 81 d after periastron, and compare well against the smoothed particle hydrodynamics (SPH) model of Okazaki et al. (2008).

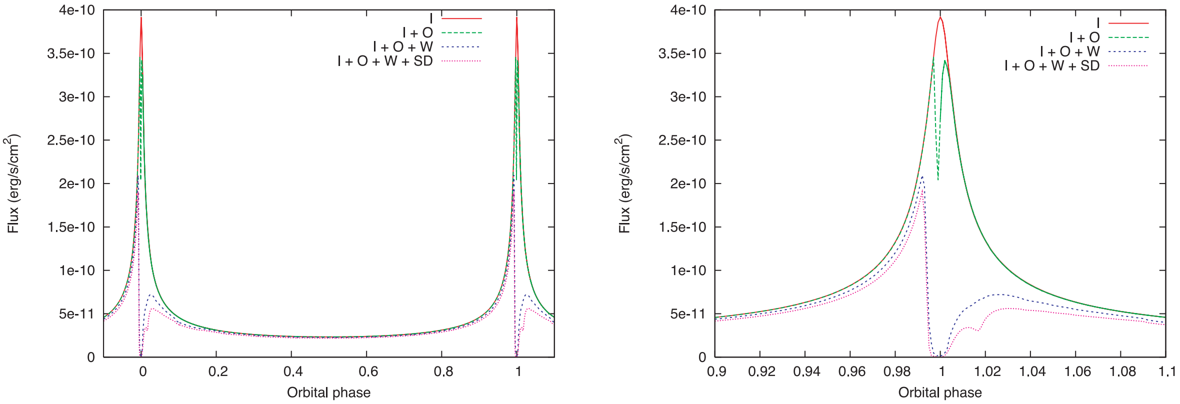

Figure 4. The effect of various attenuation mechanisms on the observed 2–10 keV emission as a function of orbital phase over an entire orbital period (left-hand panel), and over the orbital phase range 0.90–1.10 (right-hand panel). The unattenuated intrinsic emission (I) is shown by the solid red curve. Various attenuation mechanisms are then sequentially added: occultation (O), wind attenuation (W) and attenuation through the thin dense post-shock primary wind layer (SD). The viewing angles for these curves are $i = 90°$ and $\theta = 0°$, with the other model parameters listed in Table 1. The aberration of the WCR due to orbital motion and interstellar + nebula absorption (1×10^{22} cm^{-2}) are included.

observable X-ray emission originates from the post-shock secondary wind although mixing at the CD due to dynamical instabilities (PC02; see also Fig. 17) is a complicating factor. Note that lower values of χ_2 at periastron indicate that cooling may be important for a short period (Fig. 16), especially if the secondary wind is clumpy and/or if radiative inhibition reduces its pre-shock speed. These possibilities are investigated in more detail in Section 5. In the meantime, we assume that the shocked secondary's wind is adiabatic throughout the entire orbit, emits the entirety of the X-ray emission, and that the intrinsic X-ray luminosity scales as $1/d_{\rm sep}$, where $d_{\rm sep}$ is the stellar separation (Stevens et al. 1992; Pittard & Stevens 1997).

3.2 Attenuation

The intrinsic X-ray emission is attenuated by the unshocked winds. In wide binaries one can usually assume that the winds are instantaneously accelerated. However, in η Car the primary's wind may accelerate very slowly and this may affect the degree of attenuation observed. When describing the wind acceleration using a β velocity law, a typical value for the slow acceleration of an LBV wind would be $\beta = 4$ (Barlow & Cohen 1977; Pauldrach & Puls 1990). To test whether this is an important factor we compared simulations adopting accelerating and instantaneously accelerated winds and found that the difference in attenuation was small at all phases, and for all lines of sight.

Attenuation by the shocked winds also occurs. Since the shocked secondary wind is assumed to be hot, it is also assumed to have negligible attenuation.[1] In contrast, the dense, cool layer of post-shock primary wind is a significant source of absorption. The surface density (SD) of this layer changes by over two orders of magnitude between periastron and apastron ($\sigma \propto d_{\rm sep}^{-2}$), resulting in a dramatic increase in attenuation around periastron for X-rays. For viewing angles closely tangential with the shock surface the combination of the increased post-shock gas density and the path-length-dependent absorption described in PP08 is sufficient to fully absorb X-rays with energies $\lesssim$4 keV.

3.3 Observed emission

Prior to modelling the *RXTE* light curve, we explore the effect on the observed X-ray light curve of including various occultation and attenuation mechanisms. A light curve from a model with the parameters listed in Table 1 and viewing angles $i = 90°$, $\theta = 0°$ is shown in Fig. 4. The skew of the WCR due to orbital motion causes the minimum to be asymmetric, as observed. A particularly interesting feature is the shoulder seen on the egress out of minimum.

---

[1] This is a suitable assumption for the purposes of our model; however, it has been suggested by Henley et al. (2008) that attenuation by the companion wind plays a role in shaping the emission line profiles.

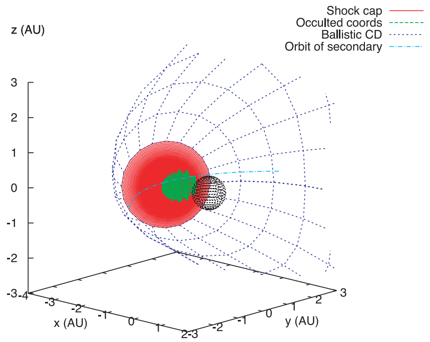

Figure 5. A 3D plot of the occultation of the WCR by the primary star at periastron ($\phi = 0.0$) with $e = 0.9$ and a viewing angle of $i = 90^\circ$ and $\theta = 0^\circ$. The region occulted by the primary star (displayed in black) is shown in green. Although the primary star is directly in front of the secondary star for the chosen values of i and θ, due to aberration the shadow does not fall directly on the apex of the WCR.

This is caused by attenuation through the dense layer of shocked primary wind (see below).

Occultation by the primary star (Fig. 5) causes a considerable reduction in emission around periastron though the effect is very short-lived and does not cause the observed minimum (see Fig. 4). Instead, the largest source of attenuation arises from the unshocked stellar winds except for a phase interval of ≈0.01 during the minimum when absorption through the shocked primary wind dominates (Fig. 6). The smallest values of the emission weighted column (PP08) occur at apastron, when the sightlines from the head of the WCR initially pass through the secondary wind. A circumstellar column of $2 \times 10^{22}\,\mathrm{cm}^{-2}$ (the absorption from shocked and unshocked winds within the simulation box, see PP08), plus a column of $1 \times 10^{22}\,\mathrm{cm}^{-2}$ which includes absorption in the Homunculus and ISM, is sufficient to absorb ∼99.99, 90 and 20 per cent of the 1-, 2- and 5-keV X-rays from the WCR, respectively. The column density begins to increase as the stars approach periastron, then there is a dramatic rise in the column through the unshocked winds at $\phi \sim 0.99$ which highlights the shift of the lines of sight into the high-density primary wind. This is accompanied by a peak in absorption by the shocked primary wind, represented by the SD component. The two peaks in the SD component column at phases $\phi \sim 0.99$ and 1.02 are produced by sightlines originating from points with the highest intrinsic luminosity becoming closely tangential with the shock surface. The short duration in phase of the peak in column density (which briefly reaches $\sim 10^{25}\,\mathrm{cm}^{-2}$) denotes the rapid motion of the stars through periastron passage.

The attenuation along lines of sight close to the positive x-axis (i.e. $i = 90^\circ$, $\theta = 0^\circ$) at phases near apastron is composed of large volumes of unshocked secondary wind and slices of dense primary wind (cf. Fig. 2), with the former dominating.

Increasing the radius of the primary star causes the depth, and width, of the occultation component of the minimum, and the actual minimum to increase slightly, but the high eccentricity combined with the rapid orbital motion of the stars around periastron results in very little change to the attenuating column densities. The light curve is also relatively insensitive to the rate of the acceleration of the primary wind (which affects the density near to the star) and to the velocity cut at which the flow in the WCR is assumed to behave ballistically (see PP08).

4 RESULTS

4.1 Varying model parameters

In the following subsections we explore the effect of varying the orientation of the orbit, the wind momentum ratio and the eccentricity.

4.1.1 Variation with orbital inclination

Fig. 7 shows how varying the orbital inclination angle changes the observed light curve. For values of $i = 60^\circ$–90° the synthetic light curves are largely similar. For $i \simeq 45^\circ$, similar to the 42° inclination angle derived for the polar axis of the Homunculus nebula (Smith 2006), the ratio of the pre- and post-minimum X-ray emission is reduced considerably and is in much better agreement with the *RXTE* data (see also Steiner & Damineli 2004; Akashi et al. 2006; Kashi & Soker 2007; Okazaki et al. 2008). Reducing the inclination angle further to $i = 30^\circ$ causes the pre-/post-minimum flux ratio to become too small. Although reducing i decreases the direct occultation of the region of the WCR with the largest intrinsic luminosity around periastron passage (Fig. 5), the wind absorption increases as a larger fraction of the X-rays initially pass through the primary wind (cf. Fig. 7).

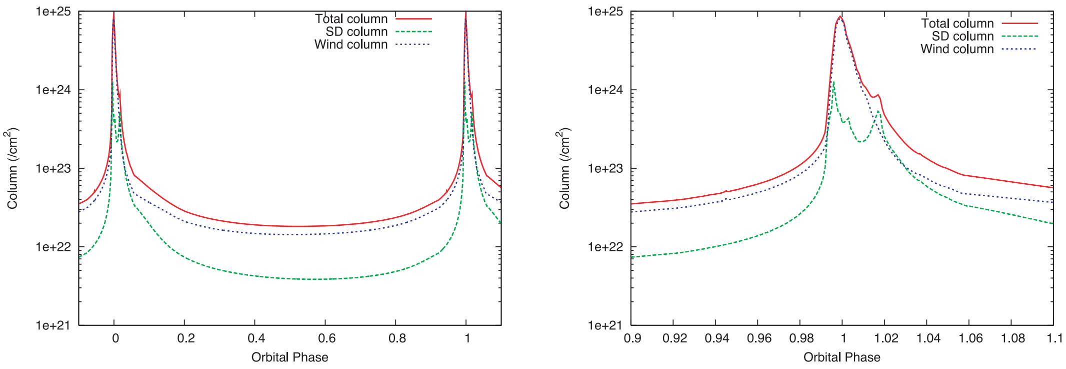

Figure 6. The effect of various attenuation mechanisms on the emission weighted column density as a function of orbital phase. The total column (red), attenuation due to the unshocked stellar winds (blue) and attenuation due to X-rays intersecting the dense, cold layer of post-shock primary wind (green) are shown over an entire orbital period (left-hand panel) and over the orbital phase range 0.90–1.10 (right-hand panel). Interstellar + nebula absorption ($\sim 1 \times 10^{22}\,\mathrm{cm}^{-2}$) has not been added to these plots. The viewing angles are $i = 90^\circ$ and $\theta = 0^\circ$.

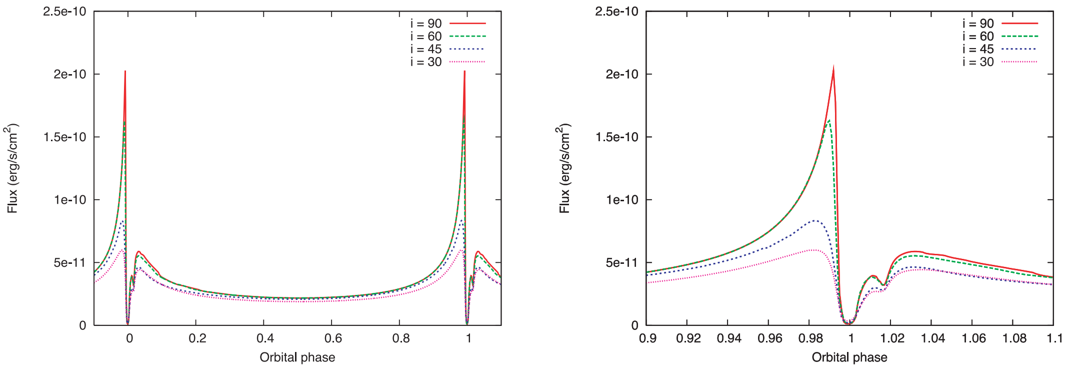

Figure 7. Synthetic 2–10 keV light curves for various inclination angles, *i*, over an entire orbital period (left-hand panel) and over the orbital phase range 0.90–1.10 (right-hand panel). An inclination angle of 45° provides the best resemblance to the observed morphology (Fig. 1). The parameters used to calculate these results are noted in Table 1. $\theta = 0^\circ$ in each of these models.

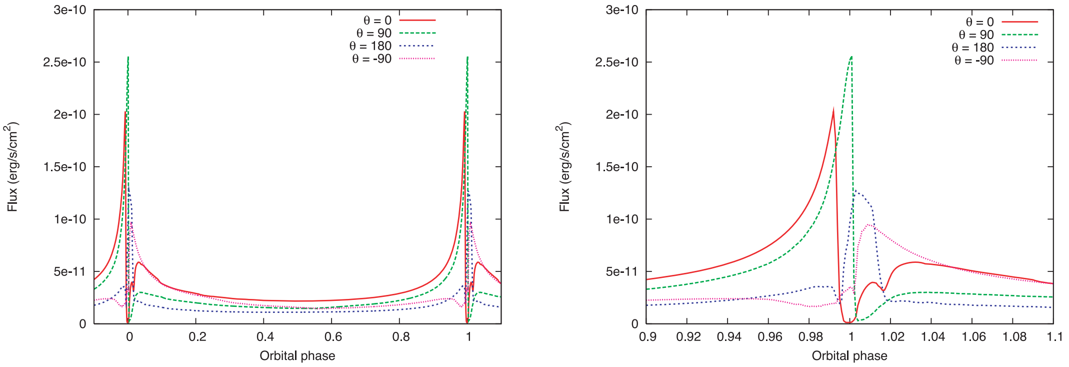

Figure 8. Synthetic 2–10 keV light curves for an inclination $i = 90^\circ$, eccentricity, $e = 0.9$, and various line-of-sight angles, θ, over an entire orbital period (left-hand panel) and over the orbital phase range 0.90–1.10 (right-hand panel). All other parameters are noted in Table 1.

4.1.2 Variation with the orientation of the orbital semimajor axis

As mentioned in Section 1, there are competing suggestions for the orientation of the semimajor axis. Fig. 8 shows the effect on the observed X-ray emission of varying the line-of-sight angle, θ, while keeping the inclination angle constant at $i = 90^\circ$. In each case, the maximum emission occurs while the sightline to the apex of the WCR is through the less dense secondary wind.

4.1.3 Variation with orbital eccentricity

For the majority of the calculations an orbital eccentricity of $e = 0.9$ was adopted. The eccentricity affects the orbital velocity of the companion star around periastron, the distance of closest approach of the stars, and the amount of time the companion star and the region of the WCR with the highest intrinsic luminosity (assuming $L_{X_{\rm int}} \approx 1/d$, but see Section 5 for caveats) spends immersed in the dense primary wind. Lowering the value of e increases the width of the minimum towards $\phi \sim 0.03$ which is desired (Fig. 9). However, the decline to minimum then occurs at earlier phases. This can be countered by increasing the value of θ (cf. Fig. 8), although there are then implications for the pre-/post-minimum luminosity ratio, and the morphology of the egress out of minimum. On the other hand, increasing the eccentricity decreases the duration of the minimum and increases the pre-/post-minimum luminosity ratio. Overall, a best fit is obtained with $e \simeq 0.9$, in agreement with previous work (e.g. Henley et al. 2008). However, if the WCR collapses at periastron (see Section 5) the eccentricity may be higher.

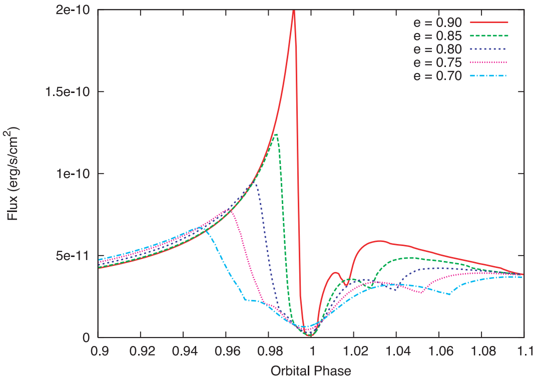

Figure 9. Synthetic 2–10 keV light curves over the orbital phase range 0.90–1.10 for $\eta = 0.24$, an inclination $i = 90^\circ$, line-of-sight angle $\theta = 0^\circ$, and varying values for e. The orbital and wind parameters used are noted in Table 1.

4.1.4 Variation with wind momentum ratio

Varying the momentum ratio between the winds (by adjusting $\dot{M}_1$) affects the opening angle of the WCR and the spatial distribution of the unshocked winds, and changes the attenuation and observed X-ray emission, as shown in Fig. 11. Decreasing η causes the sightlines to the apex of the WCR to move into the denser LBV wind at earlier orbital phases, and produces a wider minimum at periastron. When $\eta = 0.024$ the opening angle of the WCR is reduced so much that the sightline from the WCR apex moves into the primary wind at such an early phase that a significant rise in X-ray luminosity before periastron is prevented. Another effect of reducing η is that more of the secondary wind becomes shocked in the WCR. This means that the luminosity at apastron initially increases as η decreases from 0.24. However, the opening angle of the WCR soon decreases to such an extent that sightlines to the apex of the WCR move into the primary wind, so that the luminosity at $\phi = 0.5$ declines for $\eta \lesssim 0.04$.

With $\dot{M}_1 = 3.5 \times 10^{-3}\,\mathrm{M}_{\odot}\,\mathrm{yr}^{-1}$ (and $\eta = 0.024$) the peak column density at periastron increases to $\simeq 2 \times 10^{25}\,\mathrm{cm}^{-2}$ (Fig. 12). The X-ray minimum is flat and has approximately the correct width ($\delta\phi \sim 0.03$, corresponding to 60 d), yet, the decline to, and egress out of, minimum are too shallow, and the rest of the light curve is a poor match to the observations. If increased mass-loss is responsible for the flat bottom of the minimum, Fig. 11 shows that it must be confined to a short phase interval around periastron (see also Corcoran et al. 2001). The effect of a short-lived episode of increased mass-loss is discussed further in Section 5.

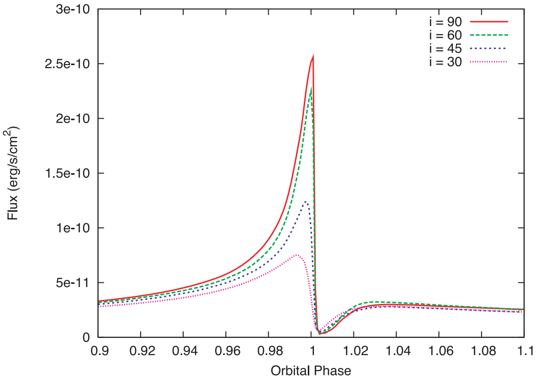

Figure 10. Synthetic 2–10 keV light curves for $\eta = 0.24$, line-of-sight angle $\theta = 90^{\circ}$, eccentricity $e = 0.9$, and varying inclination angle, i, over the orbital phase range 0.90–1.10. The orbital and wind parameters used to calculate these results are noted in Table 1. Comparison with Fig. 1 shows that these curves do not reproduce the observed light curve.

4.2 Comparison to the X-ray data

In the following subsections we examine fits to the *RXTE* light curve and hardness ratio, and *XMM–Newton* spectra.

4.2.1 *Fits to the RXTE light curve*

Having explored how the light curves vary with i, θ, e and η, we performed further simulations to obtain a best fit to the *RXTE* data. The binary models of Abraham et al. (2005) and Henley et al. (2008) suggest $i \simeq 90^{\circ}$ and 70°, respectively. However, for such values we find a strong disagreement between the *RXTE* and synthetic light curves, mainly due to the large difference between the pre- and post-minimum X-ray luminosities in the model light curves. A comparison of the $\theta = 180^{\circ}$ curve in Fig. 8 and the *RXTE* data shows that an orientation where the secondary star is in front of the primary during periastron passage (Falceta-Gonçalves et al. 2005; Kashi & Soker 2007) is not supported. Smith et al. (2004) suggested that $\theta = 90^{\circ}$. However, the required pre-/post-minimum flux ratio, and duration of the minimum, cannot be obtained with any sensible inclination angle when $\theta = 90^{\circ}$, as shown in Fig. 10. Instead, the *RXTE* data require the observer to be situated close to the semimajor axis with $\theta \simeq 0^{\circ}$ (e.g. Damineli 1996; Pittard et al. 1998; Corcoran et al. 2001; Corcoran 2005; Akashi et al. 2006; Hamaguchi et al. 2007; Nielsen et al. 2007; Damineli et al. 2008b; Henley et al. 2008), whereby the companion star moves behind the primary at periastron or just after. A detailed analysis of parameter space using 'chi-by-eye' yields best-fitting values of $i \simeq 42^{\circ}$ and $\theta \simeq 20^{\circ}$, in good agreement with Okazaki et al. (2008).

A good match to most of the light curve is obtained with $i = 42^{\circ}$, $\theta = 0$–30°, $\eta = 0.18$ and $e = 0.9$ (see Fig. 13), though a flat extended minimum cannot be produced. Interestingly, Corcoran (2005) and Hamaguchi et al. (2007) discussed two phases to the minimum; an initial deep minimum and a shallower phase which begins approximately halfway through. This behaviour is seen in the model light curves and can be understood by examining Figs 6 and 12, which show a step in the emission weighted column density due to absorption by the cooled post-shock primary wind exceeding the absorption through the unshocked winds. Note that this step is not visible in the $\eta = 0.024$ light curve in Fig. 11 as the attenuation due to the unshocked winds always dominates.

The similarity between the model and *RXTE* light curves with $\eta = 0.18$ shows that the system can be described well for the majority of the orbit with one set of parameters. However, the exact shape of the minimum could not be matched with any single set of mass-loss rates and terminal wind speeds. In particular, the absorption peak (Fig. 12) does not have the necessary duration to create a flattish minimum. The steep rise out of minimum observed by *RXTE* also cannot be replicated. This indicates a need for some additional physics around periastron passage which causes the column to stay at $\sim 10^{25}\,\mathrm{cm}^{-2}$ until $\phi \sim 1.03$ (*XMM–Newton* observations find the column to be $\gtrsim 10^{23}\,\mathrm{cm}^{-2}$ over this phase range) or some physical process to reduce the intrinsic emission. A number of mechanisms which could effect the structure of the WCR and the observed emission are discussed in Section 5.

Since the intrinsic X-ray luminosity scales as $L_{\mathrm{X}} \propto \dot{M}^2$ in our model (where it is assumed that the post-shock secondary wind is adiabatic), the normalization of the light curve can indicate the mass-loss rates of the stars. We find that when model light curves produced with the wind parameters in Table 1 are compared to the *RXTE* data the normalization of the model is a factor of $\simeq 2.2$ too low, which for fixed η corresponds to an underestimate in $\dot{M}_2$ of $\simeq 1.5$. Various factors contribute to this discrepancy, such as the distance to the source and the interstellar column adopted in the calculations compared to those of PC02, who assumed a distance to η Car of 2.1 kpc, and obtained a combined circumstellar and interstellar column density of $\simeq 7.7 \times 10^{22}\,\mathrm{cm}^{-2}$. In contrast, this paper adopts an interstellar + nebula column of $1 \times 10^{22}\,\mathrm{cm}^{-2}$ (the majority of which being due to the Homunculus nebula as the ISM column density is only $\simeq 3 \times 10^{21}\,\mathrm{cm}^{-2}$) and a distance of 2.3 kpc (determined from long-slit spectroscopic observations with the *HST* by Hillier et al. 2001). In addition, the lack of spatial resolution with *RXTE* will lead to additional 2–10 keV flux from nearby, unresolved sources, including the constant components identified by Hamaguchi et al. (2007). In order to compare like-with-like a background spectrum of these unresolved sources has been added to all of the model light curves where a direct comparison is made against *RXTE* data, e.g. Figs 13, 14 and 24. Despite this addition, a small discrepancy remains, and slightly larger $\dot{M}$ values ($\dot{M}_1 = 4.7 \times 10^{-4}\,\mathrm{M}_{\odot}\,\mathrm{yr}^{-1}$ and $\dot{M}_2 = 1.4 \times 10^{-5}\,\mathrm{M}_{\odot}\,\mathrm{yr}^{-1}$) than

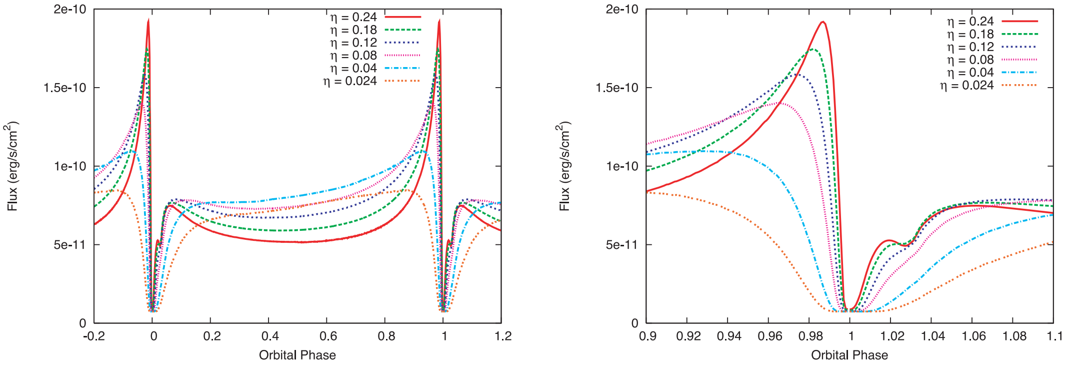

Figure 11. Variation of the attenuated 2–10 keV X-ray emission for $e = 0.9$, $i = 42°$, $\theta = 20°$ and varying values of the wind momentum ratio η shown over the whole orbit (left-hand panel) and over the orbital phase range 0.90–1.10 (right-hand panel). The orbital and wind parameters are noted in Tables 1 and 2.

Table 2. Parameters used for the models shown in Figs 11 and 12. In all simulations the terminal velocity of the primary, $v_{\infty 1}$, and secondary, $v_{\infty 2}$, star's winds are 500 and 3000 km s^{-1}, respectively.

η	$\dot{M}_1$ ($M_\odot$ yr^{-1})	$\dot{M}_2$ ($M_\odot$ yr^{-1})
0.24	3.5×10^{-4}	1.4×10^{-5}
0.18	4.7×10^{-4}	1.4×10^{-5}
0.12	7.0×10^{-4}	1.4×10^{-5}
0.08	1.1×10^{-3}	1.4×10^{-5}
0.04	2.1×10^{-3}	1.4×10^{-5}
0.024	3.5×10^{-3}	1.4×10^{-5}

determined by PC02 are required to bring the model results into agreement with observations.

4.2.2 *The hardness ratio*

A comparison of the hardness ratio from the best-fitting $\eta = 0.18$ model and the *RXTE* data is shown in Fig. 14. We find there is a good agreement between the model and the *RXTE* data for large parts of the orbit. The model hardness ratio initially rises towards periastron as stronger absorption preferentially reduces the soft-band flux. This rise is also seen in the *RXTE* data. However, the most noticeable feature in the *RXTE* data is a sudden softening of the flux which lasts throughout the X-ray minimum. In contrast, the model flux is hard for the duration of the X-ray minimum, except for a brief period when the head of the WCR is occulted by the primary star. The lack of agreement between the data and the model indicates that the X-ray minimum is not solely caused by absorption and occultation effects. Instead, there appears to be a substantial intrinsic reduction of the hardest emission in the *RXTE* data during the minimum. As we shall see, this also helps to explain the discrepancy which exists between the light curves in Fig. 13. The observational data used to calculate the hardness ratio include emission from prominent background sources in the *RXTE* field of view such as W R 25 and Trumpler 14 and 16. The flux from these sources is predominantly in the soft band and accounts for the fact that although the $\phi = 1.009$, 1.015 and 1.023 spectra from η Car shown in Fig. 15 clearly have higher hard band flux than soft band, the softening in the *RXTE* data may be due to imperfect accounting for the soft X-ray background.

An interesting result is that there is a softening in the observed flux from η Car after phase $\phi \sim 2.1$, which is highlighted by the fact that although the *RXTE* data appear very similar through both cycles there is a noticeable difference between the model and the data when both have the detector response included. This is suggestive of an intrinsic variation in the source of the emission, but uncertainties in the assumed PCU detector response in the 2–10 keV band cannot yet be ruled out.

4.2.3 *The X-ray spectra*

A series of *XMM–Newton* observations obtained through the 2003 periastron passage have been analysed by Hamaguchi et al. (2007).

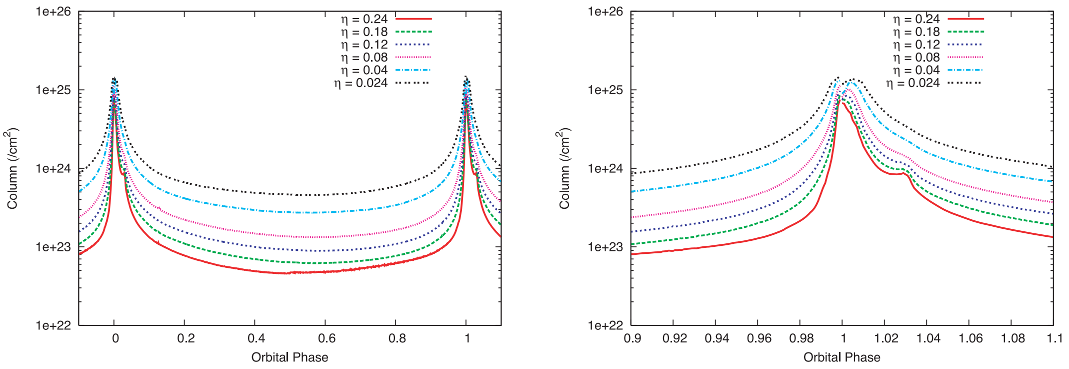

Figure 12. Variation of the emission weighted column density (cm^{-2}) for $\eta = 0.24$, 0.18, 0.12 and 0.024, with $e = 0.9$, $i = 42°$, $\theta = 20°$ shown over the whole orbit (left-hand panel) and over the phase range 0.9–1.1 (right-hand panel). The interstellar + nebula column ($\sim 1 \times 10^{22}$ cm^{-2}) are additional to these plots.

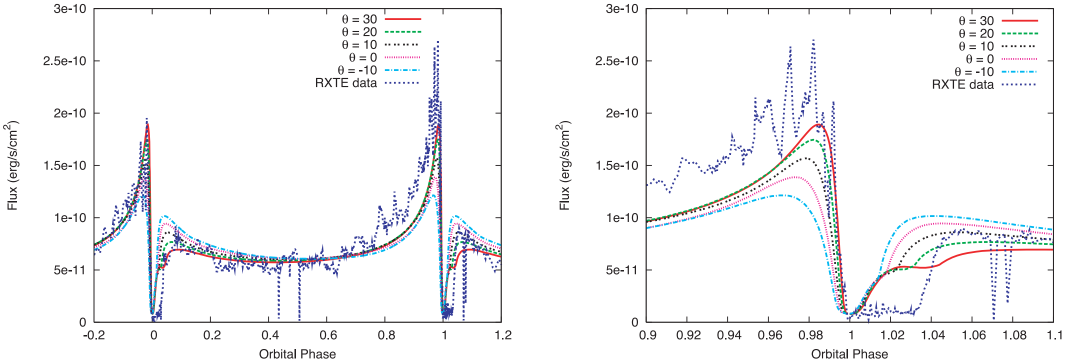

Figure 13. Variation of the attenuated 2–10 keV X-ray emission for $\eta = 0.18$, $e = 0.9$, $i = 42°$, and values of θ of $-10°$ to $30°$ in increments of $10°$ over the whole orbit (left-hand panel) and over the orbital phase range 0.90–1.10 (right-hand panel). The orbital and wind parameters used are noted in Tables 1 and 2. The model results are plotted against the second orbit *RXTE* data (which has a higher pre-minimum flux than the first orbit data, see e.g. Figs 1 and 24) for comparison.

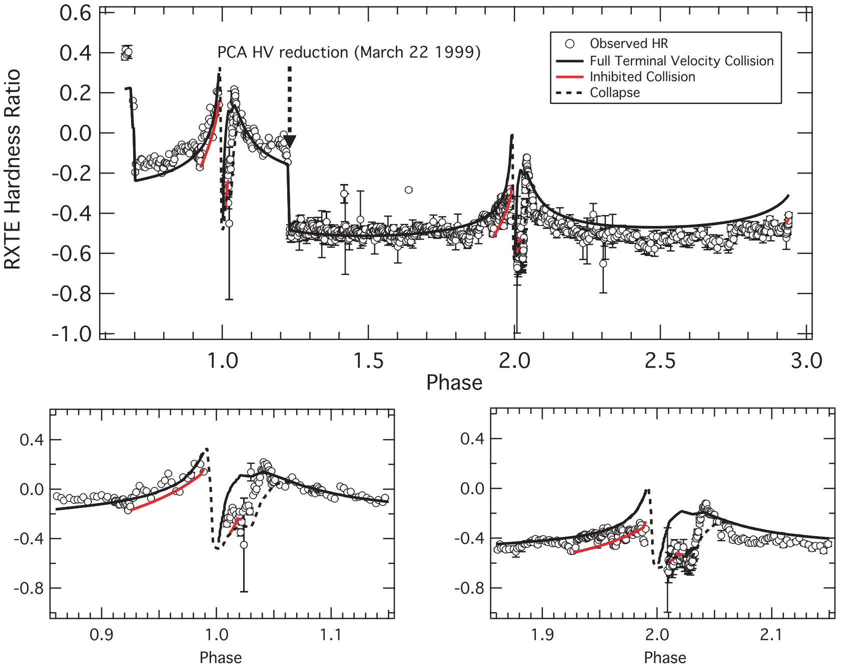

Figure 14. Variation of hardness ratio with phase for the best-fitting $\eta = 0.18$ model and the *RXTE* data over the 2.5 orbits. The model hardness ratio has had the detector response folded in for each specific observation. Due to fluctuations in the calibrated channel energy gains there is some jagged structure to model hardness ratio leading up to periastron passage. The large drop at $\phi = 1.23$ corresponds to a gain reduction in the PCU onboard *RXTE*, and is also incorporated in the folded model. The change at $\phi = 0.7$ is due to a change in the detector response model. The soft band (s) is 2–5 keV, the hard band (h) is 7–10 keV, and the ratio is calculated as $\mathrm{hr} = (h - s)/(s + h)$. The dip in the model ratio at periastron is due to occultation of the WCR by the primary star. Over the orbital phase range $0.924 \lesssim \phi \lesssim 1.023$ and $1.924 \lesssim \phi \lesssim 2.023$ the hardness ratio values are from the individual models with lower companion wind velocities, discussed in Section 5.2, are shown (red). In the $2.0 \lesssim \phi \gtrsim 3.0$ cycle the model appears softer than in the previous cycle; however, this is the result of processing the model data with the detector response.

The observed spectra are a combination of a variable hard component originating from the WCR, and a number of other non-variable components. The *XMM–Newton* spectra in Fig. 15 have the non-variable emission components from the outer ejecta, the X-ray Homunculus nebula, and the central constant emission component identified by Hamaguchi et al. (2007) removed. These spectra are compared to those produced from our best model fit to the *RXTE* light curve. The Fe line at ∼7 keV has a large fluorescence component which is not modelled in the synthetic spectra; the goal of this paper is to reproduce the broad-band spectra, and not the lines. Recently, Behar, Nordon & Soker (2007) and Henley et al. (2008) examined the variability of the sulphur and silicon emission to study the flow dynamics within the WCR. Future work will focus on developing the dynamic model to perform individual studies of spectral lines.

At $\phi = 0.924$ we find that there is a significant deficiency in the emission from our 'standard' model (with $v_{\infty 2} = 3000\,\mathrm{km\,s^{-1}}$) at the softer end of the spectrum ($E = 1$–$4\,\mathrm{keV}$). Thus the model spectrum is slightly harder than the data, indicating that the post-shock temperature of the companion's wind is overestimated. The temperature reduction in the post-shock companion wind could be partly caused by mixing of the cold post-shock primary wind into

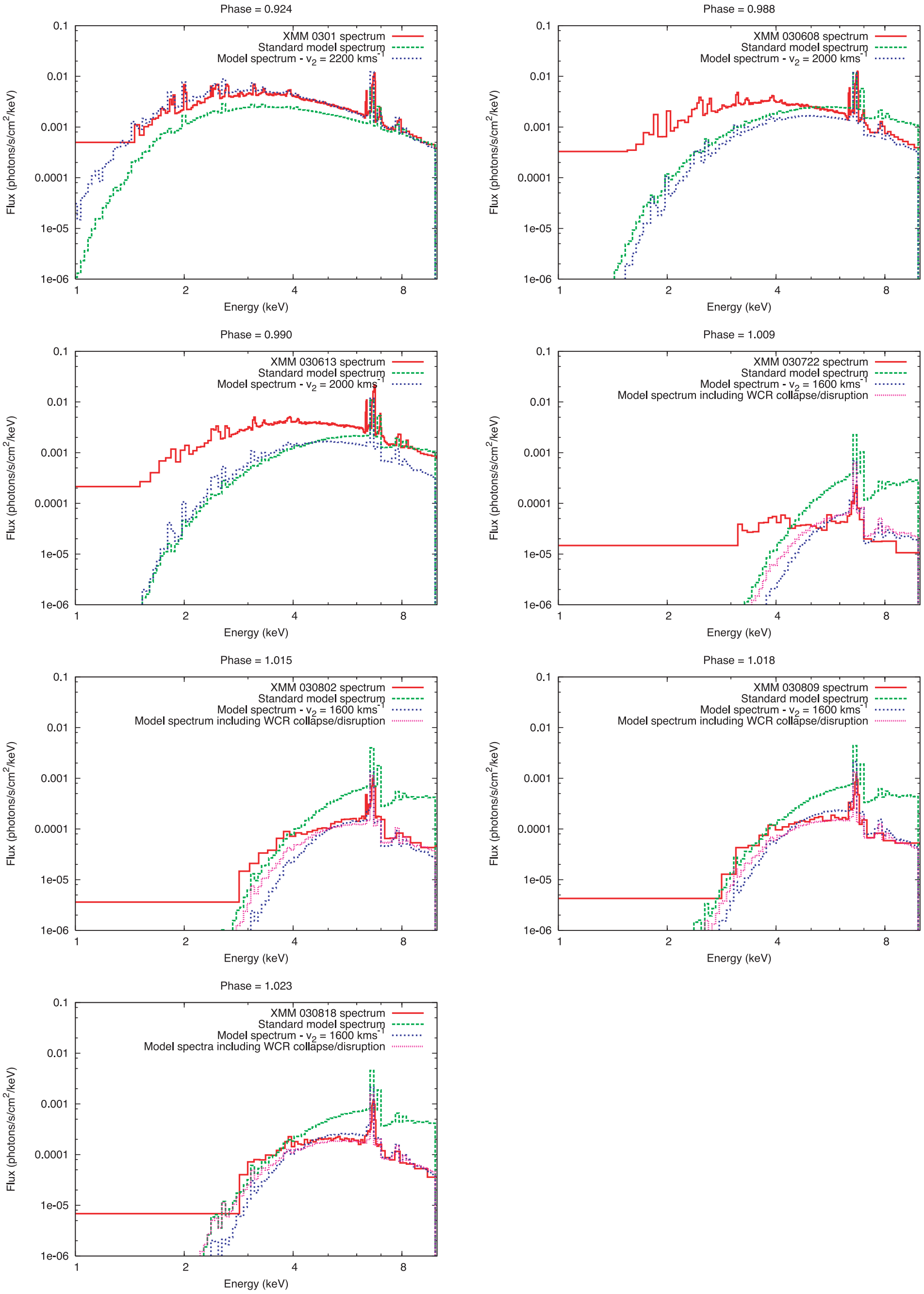

Figure 15. 1–10 keV model spectra with $\eta = 0.18$, $i = 42^\circ$ and $\theta = 20^\circ$ plotted against *XMM–Newton* data (see Hamaguchi et al. 2007) as a function of phase. In the ‘standard’ model the companions wind is assumed to have a pre-shock speed of $3000\,\mathrm{km\,s^{-1}}$. Results are also shown for models with a reduced pre-shock companion wind velocity. A model which includes a collapse/disruption of the WCR is also included in the panels at phases $\phi = 1.009$, 1.015, 1.018 and 1.023. Models with lower wind speeds or a collapse of the WCR match the observed flux above 5 keV during the minimum much better.

the hot post-shock secondary wind, which softens the spectrum, or radiative inhibition (see Section 5.2). An alternative explanation is that efficient particle acceleration causes a weaker subshock (cf. Pittard & Dougherty 2006). Strong evidence for particle acceleration in η Car has recently been presented by Leyder, Walter & Rauw (2008), who detected a hard X-ray tail ($E \sim 10$–30 keV). Including the effects of efficient particle acceleration in the models used in this paper is beyond the scope of the current work. The $\phi = 0.988$ spectrum occurs at the onset of the minimum. Although the stars are close at this point, it is still unlikely that the WCR has entered the acceleration region of the companion’s wind ($d_{\mathrm{sep}} \simeq 3.7$ au for $a = 16.64$ au and $e = 0.9$ cf. Fig. 20).

The quasi-periodic ‘flares’ observed in the *RXTE* light curve (Corcoran 2005) are not reproduced in the synthetic data. These may result from dynamic instabilities in the WCR or stellar winds and cannot be reproduced in the dynamic model used in this paper which is assumed to have a stable WCR. The *XMM–Newton* observations at $\phi = 0.988$ and 0.990 occur at the bottom and top of a flare peak, respectively, which accounts for some of the discrepancy seen between the data and model spectra.

The spectra from the ‘standard’ model at $\phi = 1.009$, 1.015, 1.018 and 1.023 also show significant excess flux at high energies.

5 THE NATURE OF THE X-RAY MINIMUM

In the previous section model simulations were performed which provided a reasonable fit to the light curve as a whole but did not give a good fit to the minimum. A detailed examination of the spectrum and hardness ratio around the minimum showed some significant discrepancies between the model results and the observations, with the model emission generally harder than the data during the minimum. In this section possible solutions for resolving this discrepancy are discussed.

A plausible scenario is that around periastron the pre-shock speed of the secondary wind is reduced to the point that it does not shock to high enough temperatures to produce the hard X-ray emission which is normally seen. This change in the pre-shock velocity may be initiated by the WCR moving into the acceleration zone of the secondary wind due to the high orbital eccentricity, or to a period of enhanced mass-loss from the primary star. Alternatively the acceleration of the secondary wind may be inhibited towards the primary star by its enormous radiation field. In addition, the shocked secondary wind may become radiative around periastron (especially if radiative inhibition is a strong effect). If both winds strongly cool, it is possible that the WCR disrupts and breaks up into a mass of cold dense blobs, each surrounded by oblique shocks as they are impacted by the supersonic winds (i.e. the WCR ‘discombobulates’ – Kris Davidson, personal communication). The fast companion wind may then be slowed through a sequence of oblique, radiative shocks, each with a lower post-shock temperature than would be obtained behind a single global shock.

However, the above processes by themselves cannot account for the long duration of the minimum, and the real picture is likely to be even more complicated. There is a possibility that the WCR collapses on to the surface of the secondary star during the close approach of the stars around periastron. This collapse would be initiated by the winds failing to attain a stable momentum balance at some point. Hydrodynamic simulations of a collapse of the WCR in the ι Orionis system (Pittard 1998) lead to a minimum in the flux and temperature of the X-ray emission at periastron (Pittard et al. 2000). A similar event may occur in the η Car system. In both the ‘collapse’ and ‘discombobulation’ scenarios mentioned above, it may take some considerable time to re-establish a bona fide WCR.

5.1 Effects of wind acceleration and variable mass-loss

The models in Section 4 have been made with the assumption that the winds collide at terminal velocity. In reality it is likely that one, or both, of the winds may still be accelerating when they collide. To gauge how this affects the previous results, the position of the stagnation point has been computed using β velocity laws for both winds, with $\beta = 4$ and 1 for the primary and secondary winds, respectively. Compared to the terminal winds case, ram-pressure balance occurs closer to the primary star at all orbital phases (since its wind accelerates more slowly). For instance, at $\phi = 1.0$ the pre-shock primary wind only reaches a velocity of $v_1 = 125\,\mathrm{km\,s^{-1}}$ and ram-pressure balance occurs at a distance of $0.44\,d_{\mathrm{sep}}$ from the companion star, compared to $0.30\,d_{\mathrm{sep}}$ when terminal velocity winds are assumed. Cooling parameters for both winds were then calculated. As expected, the primary’s wind was found to be highly radiative throughout the orbit ($\chi \ll 1$). Interestingly, the cooling parameter of the shocked companion wind at periastron is at roughly the point that cooling starts to become non-negligible ($\chi \sim 3$–5 see Fig. 16).

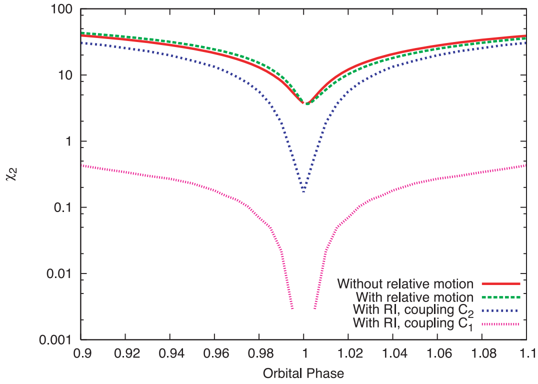

Figure 16. Variation of the cooling parameter, χ_2, for the companion wind in the orbital phase range $\phi = 0.9$–1.1. Results are shown for calculations with (green) and without (red) the inclusion of the relative motion of the stars, which affects the position of the ram-pressure balance and the pre-shock wind speeds. Prior to periastron the stars approach each other, and the relative wind speeds are higher, increasing χ compared to the static case. The opposite effect occurs after periastron. Both curves reach a minimum at periastron. For simplicity the skew of the WCR due to orbital motion is neglected, and the wind is assumed to be perfectly smooth. Clumping and efficient particle acceleration (see e.g. Pittard & Dougherty 2006) will reduce χ_2 below the level shown. The effect on χ_2 due to radiative inhibition is also shown (see Section 5.2).

Table 3. The effect of increasing the primary star mass-loss rate on the pre-shock wind speeds (v_1 and v_2), the effective momentum ratio along the line of centres (η_{loc}), the distance of the stagnation point from the centre of the companion star (r_2), and the cooling parameter of the secondary wind (χ_2). v_1 and v_2 are calculated using β velocity laws ($v_{\infty 1} = 500\,\mathrm{km\,s^{-1}}$, $v_{\infty 2} = 3000\,\mathrm{km\,s^{-1}}$, $\beta_1 = 4$ and $\beta_2 = 1$). $\dot{M}_2 = 1.4 \times 10^{-5}\,\mathrm{M_{\odot}\,yr^{-1}}$ in all models (as determined in Section 4.2.1) and the assumed stellar separation is $d_{\mathrm{sep}} = 359\,\mathrm{R_{\odot}}$ (corresponding to periastron in our standard model with $e = 0.9$). The radius of the gravitationally bound core of the primary star is taken to be $100\,\mathrm{R_{\odot}}$. η_{loc} and χ_2 are evaluated using the pre-shock, rather than the terminal, wind speeds along the line of centres. The orbital aberration of the WCR is neglected for simplicity.

$\dot{M}_1$ ($\mathrm{M_{\odot}\,yr^{-1}}$)	v_1 ($\mathrm{km\,s^{-1}}$)	v_2 ($\mathrm{km\,s^{-1}}$)	η_{loc}	r_2 (d_{sep})	χ_2
5.0×10^{-4}	127	2610	0.58	0.43	3.6
1.0×10^{-3}	147	2490	0.24	0.33	2.2
2.0×10^{-3}	164	2295	0.10	0.24	1.2
3.0×10^{-3}	173	2130	0.063	0.20	0.71

Cooling of the shocked companion’s wind becomes more important if there is a period of enhanced mass-loss from the primary wind (see Table 3) since the WCR is pushed deeper into the secondary wind resulting in lower pre-shock velocities and higher densities (see Fig. 17). Note the dramatic change in the width of the post-shock secondary wind (i.e. the distance between the shock and the CD) on the line of centres as χ_2 becomes smaller. The intrinsic X-ray emission from these models is shown in Fig. 18, where two trends are noticeable. First, the total flux increases with the primary mass-loss rate since a greater portion of the secondary wind is shocked, and secondly, the emission also becomes softer, since the pre-shock secondary wind speed declines. It is clear that the net effect of increasing $\dot{M}_1$ is to increase the *intrinsic* X-ray emission,

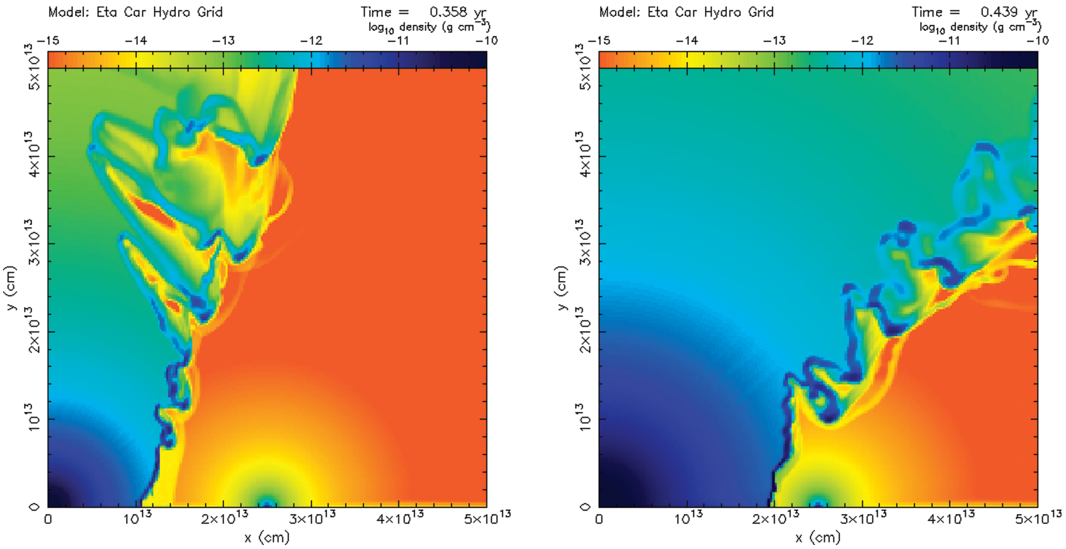

Figure 17. 2D hydrodynamic simulations of the WCR at a separation corresponding to periastron for $e = 0.9$. The plots show the effect of increasing the primary mass-loss rate ($\dot{M}_1 = 5.0 \times 10^{-4}$ (left-hand panel) and 3×10^{-3} (right-hand panel) $\mathrm{M_\odot\ yr^{-1}}$). In each simulation the wind speeds are set according to the on-axis pre-shock speed determined from a simple consideration of momentum balance (see Table 3 where the effective wind momentum ratio along the line of centres is also given). As the WCR is pushed into the acceleration zone of the secondary wind the shocked secondary wind becomes increasingly radiative ($\chi_2 = 3.6$ in the left-hand panel and 0.71 in the right-hand panel) and the WCR becomes increasingly unstable. No gravitational or radiative driving forces are included in these calculations.

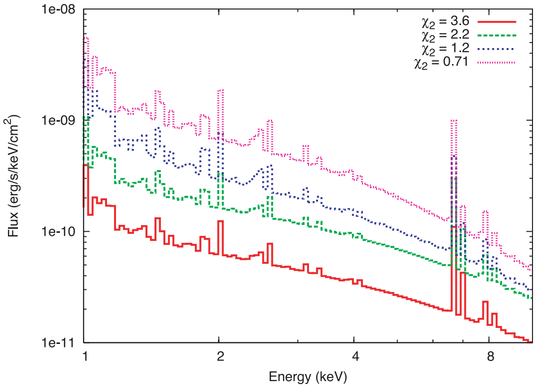

Figure 18. 1–10 keV spectra showing the variation in the intrinsic emission calculated from a 2D hydrodynamic simulation as the mass-loss rate of the primary star increases. The spectra are labelled by their respective values of χ_2, as noted in Table 3.

Table 4. The parameters used to calculate the line driving of the stellar winds, and the effect of radiative braking/inhibition. T_{cs} is the temperature at the surface of the gravitationally bound core of the star, which for the primary star is taken to be at a radius of 100 $\mathrm{R_\odot}$. k and α are the CAK line driving parameters, where subscripts 1 and 2 are used to define the coupling (C) between the winds and the radiation fields of the primary and secondary stars, respectively.

	Primary	Secondary
T_{cs} (K)	25 800	30 000
$L_*(10^6\ \mathrm{L_\odot})$	4	0.3
k	0.351	0.443
α	0.525	0.712
$\dot{M}$ ($\mathrm{M_\odot\ yr^{-1}}$)	5.0×10^{-4}	1.4×10^{-5}
v_∞(km s^{-1})	500	3000

though this would only be a temporary effect if any increase in $\dot{M}_1$ was short-lived. Any increase in $\dot{M}_1$ cannot last too long as otherwise it would lead to an observed increase in the X-ray flux as the lines of sight to the emitting plasma exit the primary wind.

5.2 Radiative braking/inhibition

The radiation fields of both stars may affect the position and nature of the WCR around periastron passage. In this section we consider two possible effects: radiative braking and radiative inhibition. The former refers to the deceleration of a stellar wind by the radiative flux from the opposing star prior to reaching the WCR, whereas the latter refers to the reduction of the net rate of acceleration of a stellar wind due to the opposing radiation field. With this in mind it is useful to note that inhibition occurs close to the star driving the wind, i.e. in the acceleration region of the wind, and braking occurs close to the WCR. To determine whether radiative braking is effective for either star, the equations of Gayley et al. (1997) have been evaluated. To perform these calculations the line driving theory of Castor, Abbott & Klein (1975) (hereafter CAK) was used to find the values of the parameters k and α required to produce the desired terminal velocities and mass-loss rates for each star (Table 4). While there is some uncertainty to the appropriate values of k and α these values provide a reasonable starting point for examining the dynamical interaction between the radiation fields and the winds in this system. We define coupling C_1 as the coupling between the primary star radiation and stellar wind, which is described by k_1 and α_1, and, respectively, coupling C_2 constitutes the equivalent for the companion star. An uncertainty in the use of the equations in Gayley et al. (1997) is that it is not clear which values of k and α should be used when considering the braking of one star's wind by the radiation field of the other (i.e. should the primary star's k and α values be used when considering braking by the secondary star's

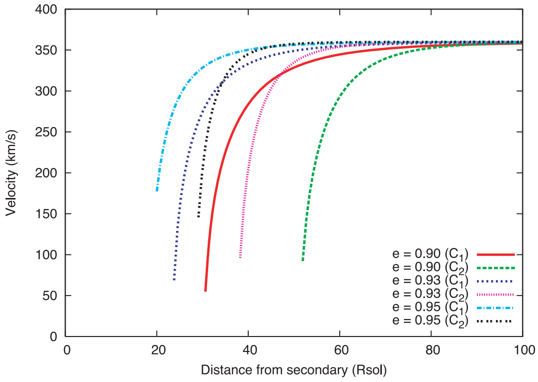

Figure 19. Radiatively braked velocity profile of the primary star's wind as it approaches the companion star for various orbital eccentricities and coupling parameters. Radiative braking causes the pronounced sudden reduction in the velocity of the incoming wind (from the right-hand side in this plot). Orbital motion is not included. The parameters used in the line driving calculations are noted in Table 4.

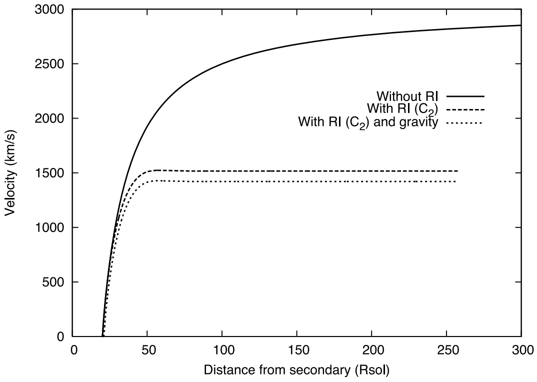

Figure 20. The speed of the companion wind towards the primary star (located at a distance of 359 $R_\odot$ which corresponds to the separation of the stars at periastron for $e = 0.9$) assuming that the coupling of the primary star's radiation field to the companion star's wind is described by coupling C_2 (i.e. the same values of the CAK parameters as required for the companion star to drive its own wind). Clearly, the acceleration of the wind is strongly inhibited by the radiation field of the primary star.

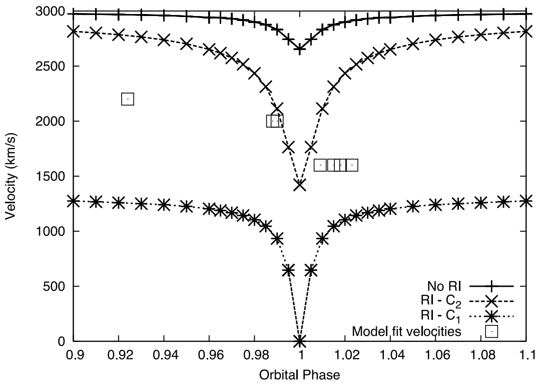

Figure 21. The pre-shock velocity of the companion's wind as a function of orbital phase for $e = 0.9$. Three scenarios are plotted: no radiative inhibition (no RI), RI with coupling C_2 (see Section 5.2) and RI with coupling C_1. The pre-shock velocity was calculated after determining the location of the stagnation point between the winds. The lower curve does not have a stable balance point at periastron, and the companion cannot launch a wind towards the primary star. Orbital motion is not included in this plot. The parameters used in the line driving calculations are noted in Table 4. The squares represent the pre-shock velocities used to attain improved fits to the *XMM–Newton* spectra in Fig. 15.

radiation? see also Pittard 1998; St-Louis et al. 2005, for further discussion). Therefore we have investigated a number of different possibilities. We find that the primary star's radiation does not brake the companion's wind, irrespective of which CAK parameters from Table 4 are used. When the close proximity of the WCR to the companion star is considered this is not such a surprising result as the ability of sudden radiative braking to halt a wind is expected to be effective when the incoming wind is close to impacting the surface of a star, which is not the case for the companion star's wind travelling towards the primary star. However, the opposite scenario of the companion's radiation field braking the incoming primary star's wind, does occur. Fig. 19 shows that in this respect alone at an orbital eccentricity of $e = 0.90$, braking is significant when the coupling is with either star (i.e. coupling C_1 or C_2). However, unless the coupling C_1 is used, the braking does not occur before the primary wind has reached the WCR. The location of sharp braking moves closer towards the secondary star as e increases, meaning that a normal ram–ram balance is increasingly likely. It is unclear whether the high density of the primary's wind will in reality prevent effective braking, as the argument of Kashi & Soker (2008) does not consider the ram pressure of the companion wind acting on the dense blobs of primary wind *and* the subsequent rate of ablation which may destroy the blobs before they reach the companion star's surface. A more in-depth examination of this mechanism is beyond the scope of this paper, but will be considered in future models. Our current calculations improve upon the approach taken by Kashi & Soker (2008) by determining the full range of coupling parameters.

As mentioned above, the radiation fields of the stars can also play a prominent role in altering the mass-loss rates and terminal velocities of the stellar winds by inhibiting the acceleration of each other's wind (Stevens & Pollock 1994). When applied to η Car we find that the radiation field of the primary star significantly reduces the terminal velocity of the companion wind (Fig. 20) to $\simeq 1520\,\mathrm{km\,s^{-1}}$ (assuming coupling C_2). A further reduction occurs if the gravitational influence of the primary star on the companion star is considered. In this case, tidal deformation results in the radius of the secondary star towards the primary increasing by $\sim 1\,R_\odot$. This in turn reduces the region available for wind acceleration, and the terminal velocity and mass-loss rate of the companion's wind drop down to $\simeq 1420\,\mathrm{km\,s^{-1}}$ and $1.25 \times 10^{-5}\,M_\odot\,\mathrm{yr^{-1}}$, respectively. When calculations are performed with coupling C_1, the companion's wind speed is significantly reduced at all orbital phases and the pre-shock velocity decreases such that a stable momentum balance cannot be attained at periastron (Fig. 21).

These alterations to the wind parameters will have drastic implications for the observed emission and may explain the wind disturbance discussed by Martin et al. (2006). To examine this scenario we have performed further hydrodynamic simulations where the wind speeds of the stars are $v_1 = 360\,\mathrm{km\,s^{-1}}$ and $v_2 = 1420\,\mathrm{km\,s^{-1}}$ (i.e. accounting for the slow acceleration of the primary wind, and the radiative inhibition of the secondary wind with coupling C_2). The shocked companion wind reaches peak temperatures of $< 10^7$ K in this case, compared to $\sim 10^8$ K if colliding at $3000\,\mathrm{km\,s^{-1}}$. The intrinsic spectra calculated from these hydrodynamic simulations are shown in Fig. 22. There is a dramatic reduction in the emission above 2 keV when the pre-shock velocity of the companion is

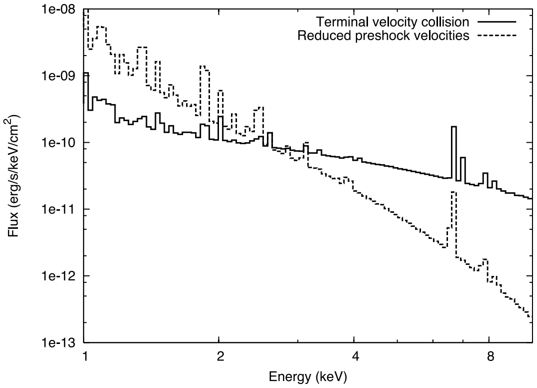

Figure 22. Intrinsic spectra calculated from hydrodynamic simulations discussed in Section 5.2 (corresponding to periastron for $e = 0.9$), where the winds are assumed to collide at terminal velocities (solid) or at much reduced velocities (dashed).

reduced to the value implied by the radiative inhibition calculations. This provides some explanation for the overestimation of the hard band flux in the dynamic model in Section 4 where terminal velocity winds are assumed (see Figs 14 and 15). Models with reduced pre-shock companion wind velocities yield much improved fits to the *XMM–Newton* spectra as shown in Fig. 15. For instance, at $\phi = 0.924$ a better fit can be attained when a pre-shock velocity of 2200 km s^{-1} is used, which indicates that radiative inhibition is important at this phase. Also, the excess in high-energy flux seen in the 'standard' model spectra at $\phi = 1.009$, 1.015, 1.018 and 1.023 can be rectified when reduced pre-shock companion wind velocities are used (a notable failing, however, is the discrepancy which still exists between the model and the data at $\phi = 0.988$ and 0.990). Interestingly, the required velocities lie within the range of predicted pre-shock velocities caused by radiative inhibition (Fig. 21). Considering the recovery of the companion wind as the stars recede, we would expect a pre-shock velocity of $v_2 \simeq 2500$ km s^{-1} at $\phi \sim 1.13$, which is significantly higher than the ~ 1100 km s^{-1} detected by Iping et al. (2005) at this phase. However, this comparison does not account for projected velocity vectors and/or the pre-shock velocity of the *downstream* gas. We note that although there is some uncertainty in the coupling parameters used, the calculations performed provide a useful guide to the range of inhibited velocities.

It is also useful to consider the degree of radiative inhibition near apastron. PC02 found a best-fitting velocity of 3000 km s^{-1}, and this value has been adopted in our 'standard' model. Reasonable agreement with this value is attained when using coupling C_2, where we find the terminal wind speed is reduced to $v_{\infty 2} = 2916$ km s^{-1}. In contrast, with coupling C_1, the companion's wind speed is more than halved giving $v_{\infty 2} = 1321$ km s^{-1}. Hence, our calculations support a coupling which is inclined towards the wind rather than the radiation field in question. At first sight this is in contrast to the findings of St-Louis et al. (2005), where the wind–wind collision in Sanduleak 1 was investigated, although their conclusion may depend on the assumed mass-loss rates. It should be noted that in reality the values of k and α are spatially and phase dependent (e.g. Fullerton, Massa & Prinja 2006; Puls et al. 2006), yet to make the problem tractable we needed to make some simplifying approximations.

Clearly, radiative inhibition is an important mechanism in the η Car system, and its effect must be properly considered in future models.

5.3 Collapse of the wind collision region on to the secondary star

Examining the ram-pressure balance between the reduced velocity winds discussed in the previous section reveals that, when $e = 0.9$, the equilibrium is stable when the companion's k and α (i.e. coupling C_2) are used in the radiative inhibition calculations (Fig. 23). An increased orbital eccentricity reduces the ram pressure of the companion's wind at periastron, due to the increasing influence of the primary's radiation field as the stellar separation is reduced. At

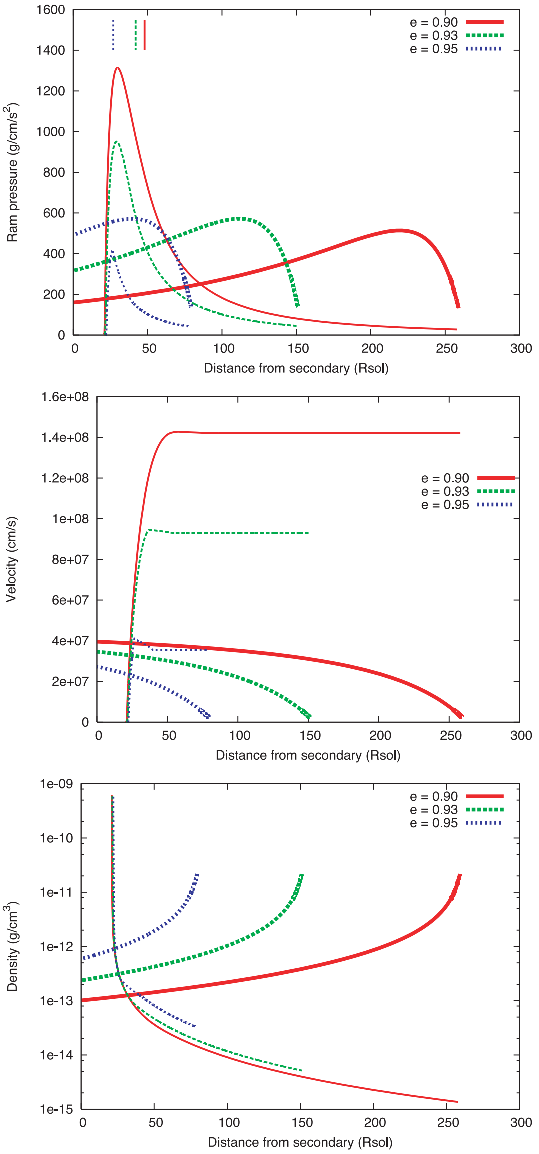

Figure 23. The ram pressure (top), velocity (middle) and density (bottom) of the radiatively driven winds as a function of distance from the companion star and orbital eccentricity. The separation of the stars corresponds to periastron in each instance. In each plot the companion's wind (thin lines) starts at 20 R$_\odot$. Radiative inhibition of the companion's wind by the primary's radiation field is included, where coupling C_2 is used. The top panel shows whether a stable momentum balance can be achieved (indicated when an intersection occurs with opposing gradients, see fig. 2 of Stevens et al. 1992). The braking radius (Fig. 19) for each scenario is indicated by the marks at the top of the uppermost plot. No stable balance exists for $e \gtrsim 0.95$ unless braking is important. The parameters used in the line driving calculations are noted in Table 4.

$e = 0.95$ there is no stable balance between the winds at periastron, which is indicated by the lack of an intersection between the ram-pressure curves for the winds with opposing gradients. If coupling C_1 is used to perform these calculations there is no stable balance point at periastron even when $e = 0.90$. Clumping within the winds, a temporary increase in the primary mass-loss rate, and the gravitational influence of the companion star may further reduce the likelihood of a stable balance between the winds. Referring back to Fig. 19 it is clear that in the scenarios where a collapse is predicted, subsequent radiative braking of the primary star's wind before it reaches the companion star's surface should also occur. This is of course a very complicated picture, and in reality it is difficult to predict the sum of all of the different mechanisms described above without a single model which self-consistently includes all of the appropriate physics which we have shown is important. This is beyond the scope of this paper, but will be addressed in future models.

Is there any observational evidence for a collapse of the WCR on to the companion star? Let us first consider the X-ray emission. While radiative inhibition can dramatically reduce the hard X-ray emission around periastron (see Fig. 22), it cannot by itself explain the long duration of the X-ray minimum and its slow recovery, since the stars separate very quickly after periastron. Furthermore, the pre-shock wind speed of the companion inferred from the fits to the *XMM–Newton* data remains roughly constant during the X-ray minimum ($\phi \simeq 1.0$–1.03), whereas the inhibition calculations indicate that it should rapidly rise (Fig. 21).

However, if the WCR collapses on to the surface of the companion star it is unclear how quickly the companion wind will be able to re-establish itself. It is entirely possible that once the primary wind collides directly with the surface of the companion star its continued ram pressure will prevent the companion star from developing a wind towards the primary star until long after periastron has passed (see the hydrodynamic simulations of such an eventuality in Pittard 1998). Indeed, the asymmetry of the X-ray minimum about periastron passage indicates that the WCR in η Car exhibits hysteresis in this sense.

To further examine this possibility a mock collapse of the WCR has been incorporated into the dynamic model in Section 4. The collapse is assumed to begin at $\phi = 1.0$ and to end at $\phi = 1.03$. The emission from the region of the WCR which is affected by the collapse is set to zero, while shocked gas further downstream (and upstream after the recovery) emits as normal. The simulated observed emission following this addition to the model is displayed in Figs 14, 15 and 24. The reduction in the hard band emission relative to the previous models is clearly evident in the spectra shown in Fig. 15, and a much better match to the observations during the minimum compared to the 'standard' model is obtained. The fit to the light-curve minimum is also considerably improved (Fig. 24). While there are remaining differences in the hardness ratio (Fig. 14), the similarity of its shape during the X-ray minimum is intriguing (specifically the slower change from softer to harder emission in the second half of the minimum). Referring back to our conclusion in Section 4.1.2 that lines of sight which favour the companion star in front at periastron are excluded still remains true in the collapse scenario as the pre-/post-minimum flux level provides a poor match to the observed light curve.

Therefore, these results provide significant support for a collapse of the WCR on to the companion star around periastron.

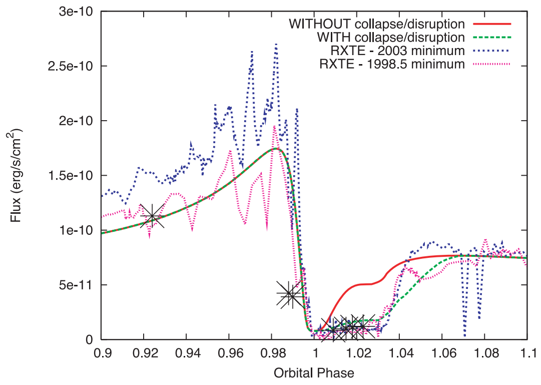

Figure 24. The 2–10 keV X-ray light curve showing the effect of a collapse of the WCR on to the companion star between phases 1.0 and 1.03. During this time the only emission arises from further downstream. The other parameters of the model are the same as those for the $\eta = 0.18$ light curve shown in Fig. 13. The crosses represent the integrated fluxes from the individual models with lower companion wind velocities discussed in Section 5.2.

During the collapse of the WCR the companion star may accrete some of the primary star wind (Soker 2005). Taking the mass accretion rate to be $\dot{M}_{\rm acc} \simeq \pi \rho_1(r) R_{\rm acc}^2 v_1(r)$ (e.g. equation 15 in Akashi et al. 2006), where $\rho_1(r)$ and $v_1(r)$ are the density and velocity profiles calculated for the primary star wind and the accretion radius[2] $R_{\rm acc} = R_2$ (Table 1). We find the total accreted mass during the collapse to be $\sim 7 \times 10^{-8}\,{\rm M}_{\odot}$, which is approximately one to two orders of magnitude lower than values noted by Kashi & Soker (2008).

6 CONCLUSIONS

We have constructed the first 3D model of the colliding winds in η Car with spatially extended, energy dependent, X-ray emission. Coriolis forces skew the WCR and wrap the far downstream regions around the stars. Attenuation of the X-rays through the unshocked winds of both stars, and through the cold, dense layer of post-shock primary wind is considered. The simulations place constraints on the orbital orientation and nature of η Car through comparison with observations from the *RXTE* and *XMM–Newton* satellites. The main findings from this paper can be summarized as follows.

(i) 3D effects, specifically the skew to the WCR due to orbital motion, lead to an asymmetry of the X-ray luminosity either side of the minimum. Circumstellar absorption is usually dominated by the unshocked stellar winds. For a very brief period ($\delta\phi \sim 0.01$) the absorption may be dominated by material in the cold post-shock primary wind.

(ii) Inclination angles similar to the polar axis angle of the Homunculus nebula (Smith 2006) are favoured.

(iii) Orientations with the secondary star in front of the primary around periastron passage are supported. The model results favour a line of sight angled at 0°–30° to the semimajor axis in the prograde direction, in agreement with Nielsen et al. (2007) and Okazaki et al. (2008). Orientations with the secondary star in front of the primary or at quadrature during periastron passage are excluded.

(iv) With terminal wind velocities fixed at $v_{\infty 1} = 500\,{\rm km\,s^{-1}}$ and $v_{\infty 2} = 3000\,{\rm km\,s^{-1}}$ for η Car and the companion star, respectively

---

[2] In Akashi et al. (2006) the accretion radius is determined under the assumption that the companion star is not driving a wind in any direction. In contrast, we assume that the companion star drives a wind on the side facing away from the primary star, hence accretion only occurs for gas striking the near-side of the companion star and the accretion area becomes $\sim \pi R_2^2$.

(our 'standard' model), the best fit to the 2–10 keV *RXTE* light curve was obtained with mass-loss rates of $\dot{M}_1 = 4.7\times10^{-4}\,\mathrm{M_\odot\,yr^{-1}}$ and $\dot{M}_2 = 1.4\times10^{-5}\,\mathrm{M_\odot\,yr^{-1}}$. These values are similar to an earlier determination by PC02 though the mass-loss rates are slightly higher and the wind momentum ratio, η is slightly lower. This difference reflects changes in the adopted distance and interstellar absorption to the system, and to difficulties in separating other, more spatially extended, components from the large *RXTE* beam. It may also reflect the lack of mixing at the CD in the dynamic model used in this paper, compared to the hydrodynamical simulations of PC02.

(v) Significant discrepancies between the observed and 'standard' model light curves and spectra exist through the X-ray minimum. We conclude that a wind eclipse is not the sole cause of the minimum, in contrast to the recent conclusions of Okazaki et al. (2008) who modelled the X-ray emission as a mono-energetic point source and considered only the light curve.

(vi) An examination of the importance of radiative inhibition has revealed that around periastron the pre-shock velocity of the companion wind is likely to be significantly reduced. The secondary wind is then shocked to much lower temperatures and cools rapidly. As a result the hard X-ray flux is efficiently quenched. All future models must properly account for the effect of radiative inhibition.

(vii) While the hard X-ray flux can be significantly reduced during periastron passage, the long duration of the minimum after periastron when the stars are rapidly separating hints that something very extraordinary happens. We believe that the most likely explanation is the collapse of the WCR on to the companion star, perhaps helped by a short increase in the mass-loss rate of the primary wind. Incorporating a mock collapse into the model between phases 1.0 and 1.03 yields significantly better agreement between the model and data.

The dynamical model described in this paper provides insight into the role of 3D effects in highly eccentric binaries. Its failings to produce synthetic X-ray emission which is a good match to the observed data have highlighted the importance of the stellar radiation fields on the dynamics of the winds and the structure and cooling of their collision region. To advance this paper further requires 3D hydrodynamical models which incorporate cooling, gravity and the driving of the stellar winds.

ACKNOWLEDGMENTS

ERP thanks the University of Leeds for funding. JMP gratefully acknowledges funding from the Royal Society. We acknowledge the help of the *RXTE* Guest Observer Facility for supporting this paper. This research has made use of NASA's Astrophysics Data System. This research has made use of data obtained from the High Energy Astrophysics Science Archive Research Centre (HEASARC) provided by NASA's Goddard Space Flight Center.

REFERENCES

Abraham Z., Falceta-Gonçalves D., Dominici T., Caproni A., Jatenco-Pereira V., 2005, MNRAS, 364, 922
Akashi M., Soker N., Behar E., 2006, ApJ, 644, 451
Barlow M. J., Cohen M., 1977, ApJ, 213, 737
Behar E., Nordon R., Soker N., 2007, ApJ, 666, 97
Canto J., Raga A. C., Wilkin F. P., 1996, ApJ, 469, 729
Castor J. I., Abbott D. C., Klein R. I., 1975, ApJ, 195, 157 (CAK)
Corcoran M. F., 2005, AJ, 129, 2018
Corcoran M. F., Hamaguchi K., 2007, Rev. Mex. Astron. Astrofis. Conf. Ser. 30, 29
Corcoran M. F., Ishibashi K., Swank J. H., Petre R., 2001, ApJ, 547, 1034
Corcoran M. F. et al., 2004, ApJ, 613, 381
Damineli A., 1996, ApJ, 460, L49
Damineli A. et al., 2008a, MNRAS, 384, 1649
Damineli A. et al., 2008b, MNRAS, 386, 2330
Davidson K., Humphreys R. M., 1997, ARA&A, 35, 1
de Groot M., Sterken C., van Genderen A. M., 2001, A&A, 376, 224
Falceta-Gonçalves D., Jatenco-Pereira V., Abraham Z., 2005, MNRAS, 357, 895
Fullerton A. W., Massa D. L., Prinja R. K., 2006, ApJ, 637, 1025
Gayley K. G., Owocki S. P., Cranmer S. R., 1997, ApJ, 475, 786
Hamaguchi K. et al., 2007, ApJ, 663, 522
Henley D. B., Corcoran M. F., Pittard J. M., Stevens I. R., Hamaguchi K., Gull T. R., 2008, ApJ, 680, 705
Hillier D. J., Davidson K., Ishibashi K., Gull T., 2001, ApJ, 553, 837
Iping R. C., Sonneborn G., Gull T. R., Massa D. L., Hillier D. J., 2005, ApJ, 633, L37
Ishibashi K., 2001, in Gull T. R., Johannson S., Davidson K., eds, ASP Conf. Ser. Vol. 242, Eta Carinae and Other Mysterious Stars: The Hidden Opportunities of Emission Spectroscopy. Astron. Soc. Pac., San Francisco, p. 53
Ishibashi K., Corcoran M. F., Davidson K., Swank J. H., Petre R., Drake S. A., Damineli A., White S., 1999, ApJ, 524, 983
Ishibashi K. et al., 2003, AJ, 125, 3222
Kashi A., Soker N., 2007, New Astron., 12, 590
Kashi A., Soker N., 2008, New Astron., 14, 11
Leyder J.-C., Walter R., Rauw G., 2008, A&A, 477, L29
Liedahl D. A., Osterheld A. L., Goldstein W. H., 1995, ApJ, 438, L115
Martin J. C., Davidson K., Humphreys R. M., Hillier D. J., Ishibashi K., 2006, ApJ, 640, 474
Moreno E., Koenigsberger G., Toledano O., 2005, A&A, 437, 641
Nielsen K. E., Corcoran M. F., Gull T. R., Hillier D. J., Hamaguchi K., Ivarsson S., Lindler D. J., 2007, ApJ, 660, 669
Okazaki A. T., Owocki S. P., Russell C. M. P., Corcoran M. F., 2008, MNRAS, 388, L39
Parkin E. R., Pittard J. M., 2008, MNRAS, 388, 1047 (PP08)
Pauldrach A. W. A., Puls J., 1990, A&A, 237, 409
Pittard J. M., 1998, MNRAS, 300, 479
Pittard J. M., 2000, PhD thesis, Univ. Birmingham
Pittard J. M., 2007, ApJ, 660, L141
Pittard J. M., Corcoran M. F., 2002, A&A, 383, 636 (PC02)
Pittard J. M., Dougherty S. M., 2006, MNRAS, 372, 801
Pittard J. M., Stevens I. R., 1997, MNRAS, 292, 298
Pittard J. M., Stevens I. R., Corcoran M. F., Ishibashi K., 1998, MNRAS, 299, L5
Pittard J. M., Stevens I. R., Corcoran M. F., Gayley K. G., Marchenko S. V., Rauw G., 2000, MNRAS, 319, 137
Puls J., Markova N., Scuderi S., Stanghellini C., Taranova O. G., Burnley A. W., Howarth I. D., 2006, A&A, 454, 625
Smith N., 2006, ApJ, 644, 1151
Smith N., Davidson K., Gull T. R., Ishibashi K., Hillier D. J., 2003a, ApJ, 586, 432
Smith N., Gehrz R. D., Hinz P. M., Hoffmann W. F., Hora J. L., Mamajek E. E., Meyer M. R., 2003b, AJ, 125, 1458
Smith N., Morse J. A., Collins N. R., Gull T. R., 2004, ApJ, 610, L105
Soker N., 2005, ApJ, 635, 540
St-Louis N., Moffat A. F. J., Marchenko S., Pittard J. M., 2005, ApJ, 628, 953
Stahl O., Weis K., Bomans D. J., Davidson K., Gull T. R., Humphreys R. M., 2005, A&A, 435, 303
Steiner J. E., Damineli A., 2004, ApJ, 612, L133
Stevens I. R., Pollock A. M. T., 1994, MNRAS, 269, 226
Stevens I. R., Blondin J. M., Pollock A. M. T., 1992, ApJ, 386, 265
Tuthill P. G., Monnier J. D., Lawrance N., Danchi W. C., Owocki S. P., Gayley K. G., 2008, ApJ, 675, 698
van Boekel R. et al., 2003, A&A, 410, L37
van Genderen A. M., Sterken C., 2007, IBVS, 5782, 1

This paper has been typeset from a TEX/LATEX file prepared by the author.